Author(s): Kankainen, Anu; Äystö, Juha; Jokinen, Ari

Title: High-accuracy mass spectrometry of fission products with Penning traps

TOPICAL REVIEW

High-accuracy mass spectrometry of fission products with Penning traps

To cite this article: A Kankainen *et al* 2012 *J. Phys. G: Nucl. Part. Phys.* **39** 093101

View the article online for updates and enhancements.

IOP Astronomy ebooks

Part of your publishing universe and your first choice for astronomy, astrophysics, solar physics and planetary science ebooks.

iopscience.org/books/aas

TOPICAL REVIEW

High-accuracy mass spectrometry of fission products with Penning traps

A Kankainen, J Äystö[1] and A Jokinen

Department of Physics, FI-40014 University of Jyväskylä, PO Box 35 (YFL), Jyväskylä, Finland

E-mail: anu.k.kankainen@jyu.fi

Abstract

Mass measurements of fission products based on Penning-trap technique are reviewed in this article. More than 300 fission products have been measured with JYFLTRAP, ISOLTRAP, CPT, LEBIT and TITAN Penning traps with a typical precision of $\delta m/m \approx 10^{-7} - 10^{-8}$. In general, the results agree well with each other. The new data provide a valuable source of information and a challenge for the future development of theoretical mass models as well as for obtaining a deeper insight into microscopic properties of atomic nuclei as measured, for example, via key mass differentials. Shape transitions around $N = 60$, subshell closure at $N = 40$ and shell closures at $N = 50$ and $N = 82$ have been investigated in the trend of the precisely measured two-neutron separation energies. The evolution of two-neutron and two-proton shell gaps has been studied and compared to theoretical models for $Z = 50$, $N = 50$ and $N = 82$. Proton–neutron pairing effect in separation energies and odd–even staggering of masses are shortly discussed. In addition to nuclear structure, many experiments have been motivated by nuclear astrophysics.

(Some figures may appear in colour only in the online journal)

1. Introduction

Accurate mass measurements of exotic nuclei are required e.g. for studies of nuclear structure and astrophysics as well as for tests of the standard model [1, 2]. In addition to the absolute mass or binding energy determination, the first and second order differentials of the masses are often the most important indicators of local and global changes of structures [3]. Such differentials offer challenging objects for precision mass measurements of nuclear ground states and low-energy isomers. Since the accuracy of the ground state mass measurements is now approaching that of the excited states it offers interesting perspectives for studying the binding energy systematics for the excited states as well. In general, the mass measurements of neutron-rich

---

[1] Current address: Helsinki Institute of Physics, FI-00014 University of Helsinki, Finland.

nuclei far from stability require a relative precision of $\delta m/m < 10^{-6}$, corresponding to about 100 keV at $A = 100$, for probing the evolution of shell structure, collectivity and shell closures [1]. These are normally studied by using the systematics of one- and two-nucleon separation energies over long isotopic or isotonic chains. A higher accuracy of $\delta m/m < 10^{-7}$ (e.g. 10 keV at $A = 100$) is typically needed for the binding energies of extremely neutron-rich halo nuclei. Relative mass accuracies below 10^{-7} are also required for studying second-order differentials, such as odd–even staggering of binding energy related to the nature of pairing in neutron-rich nuclei [4], its possible isospin dependence and role near the neutron drip-line. The same argument holds for a specific class of double differences of nuclear masses termed δV_{pn} [5–7], which isolates the proton–neutron interaction of the last two valence protons and neutrons, and has been shown, for example, to possess correlation with octupole effects in nuclear structure [8].

Indirect applications of nuclear masses are important both in fundamental as well as in applied physics. The bulk of nuclear structure studies far from the valley of stability is still based on beta-decay spectroscopy. There, reliable data on the decay Q-values are crucial, for example, when extracting the transition strengths for individual beta transitions or analysing the delayed neutron data. Nuclear data of neutron-rich nuclides, and especially for fission products, is a crucial input for network calculations in nuclear astrophysics and nuclear-energy related applications. The latter concerns decay heat, delayed neutron emission, fission yields and isomeric yields for current and future fission reactor concepts. Also, in the nuclear security front the production of pure isomeric sources for applications such as required by the Comprehensive Test Ban Treaty Organization [9] are becoming increasingly important.

The introduction of Penning traps to radioactive isotope mass measurements has changed the scope of direct mass measurements significantly. Combining them with the buffer-gas cooling [10] in a radio frequency quadrupole (RFQ) trap has made it possible to employ very fast injection of ions into a Penning trap. When coupled to a traditional ISOL system, such as ISOLDE at CERN [11], a bottle neck has become due to slow extraction, especially for refractory elements. This problem has been solved in the ion guide isotope separator on-line (IGISOL) technique [12] and its successor technique called ion catcher. The combination of all the above mentioned approaches have opened up a possibility for high-precision mass measurements of radioactive isotopes of all chemical elements with half-lives down to less than 100 ms. In this review, we give an overview of recent mass measurements of neutron-rich nuclei produced in fission reactions and discuss their implications on nuclear structure physics.

2. Experimental method

Two main production methods have been used to provide neutron-rich nuclei in the fission product region for Penning trap mass measurements (see figure 1). They are both based on ISOL technique. The ISOLTRAP mass spectrometer [13] is coupled to the ISOLDE mass separator facility and the JYFLTRAP [14–16] is connected to the universal IGISOL mass separator [12]. ISOLDE is using high-energy proton beams to produce the wanted nuclides in fission and spallation reactions whereas the IGISOL production is based on low-energy nuclear reactions.

At IGISOL, the ions of interest are produced in proton-induced fission reactions by bombarding natural uranium target with proton or deuteron beams with energies between 20 and 30 MeV and intensity between 10 and 30 μA. The targets are 15 mg cm^{-2} thick metallic foils tilted to $7°$ angle with respect to the beam axis resulting in effective thickness of 120 mg cm^{-2}. The fission reaction products are thermalized in a helium-filled gas cell at a pressure of about 100–400 mbar. Resulting from charge-exchange processes with helium
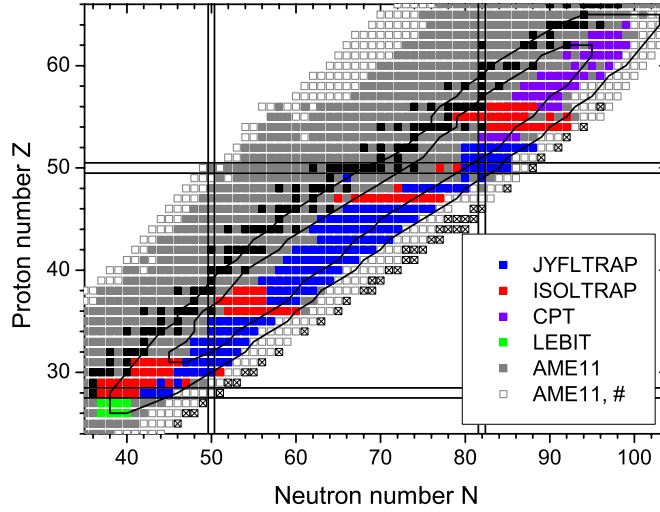
Figure 1. Chart of nuclides showing 1-μb and 1-mb contours for ^{238}U(p 25 MeV,f) and the fission fragments whose masses have been measured with Penning-traps. The nuclei for which the mass values have been extrapolated in the preview of the forthcoming AME11 [17] are denoted by open grey squares and the new nuclei identified recently at RIKEN [18] by crosses.

atoms and impurities in the gas, the majority of ions are singly charged. Fast helium flow transports the ions out of the gas cell within about 10 ms whereby they are guided through the sextupole ion guide [19] and accelerated to 30 keV energy. A combination of a 55° bending magnet and a slit allows only the ions with the selected mass number to pass towards a gas-filled RFQ cooler and buncher [20]. The RFQ cooler is used to cool and store the ions before releasing them in a short bunch into the JYFLTRAP Penning trap setup. Typical highest independent nuclide yields have been measured to be 10^5 ions s^{-1}. With the minimum required production rate of 10 ions s^{-1} about 400 short-lived neutron-rich isotopes are within reach for the mass measurement experiments with JYFLTRAP. A schematic layout of the facility is shown in figure 2.

The mass measurements of fission fragments discussed in this paper have been performed with the JYFLTRAP Penning trap [14–16] at IGISOL, ISOLTRAP [13] at ISOLDE/CERN, Canadian Penning trap (CPT) [21] at Argonne National Laboratory and LEBIT [22] at Michigan State University. Recently, some neutron-rich Rb and Sr isotopes have also been measured [23] with TITAN [24] at TRIUMF. In the following, we describe the experimental method performed at JYFLTRAP.

JYFLTRAP consists of two cylindrical Penning traps inside a 7 T superconducting solenoid. The ions in a Penning trap have three different eigenmotions: axial motion with a frequency ν_z, radial magnetron (ν_-) and reduced cyclotron motions (ν_+). According to the invariance theorem [25], the sideband frequency $\nu_- + \nu_+$ corresponds to the true cyclotron frequency with a high precision even in a non-ideal Penning trap:

$$\nu_c = qB/(2\pi m), \qquad (1)$$

where B is the magnetic field, and q and m are the charge and the mass of the ion.

The first trap of JYFLTRAP is called purification trap. It is used for beam purification via mass-selective buffer-gas cooling technique [10]. With a typical mass resolving power of around $m/\Delta m \approx 3 \times 10^4$ neighbouring isobars can usually be separated in the first trap before injecting them through a narrow diaphragm towards the second trap, precision trap. Figure 3

Figure 2. A schematic layout of the IGISOL facility.
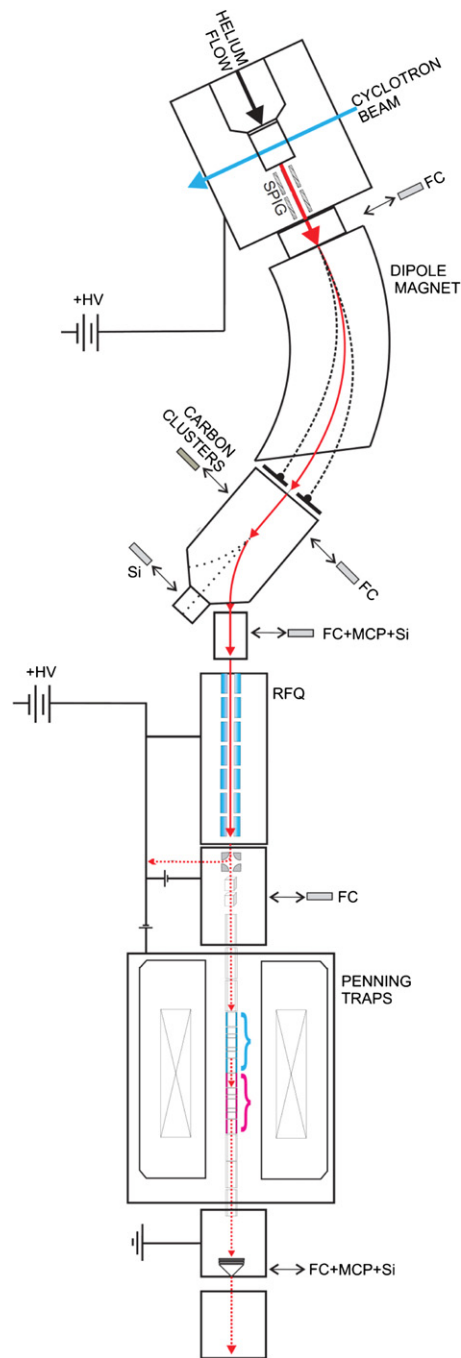
shows an example of a mass scan performed with the purification trap. Peaks corresponding to different isobars—Mo, Tc and Ru—are clearly visible and separable. By setting a correct first trap frequency only the ions of interest can be selected for precision mass measurements or the ions can be sent through the second trap for e.g. post-trap spectroscopy measurements.
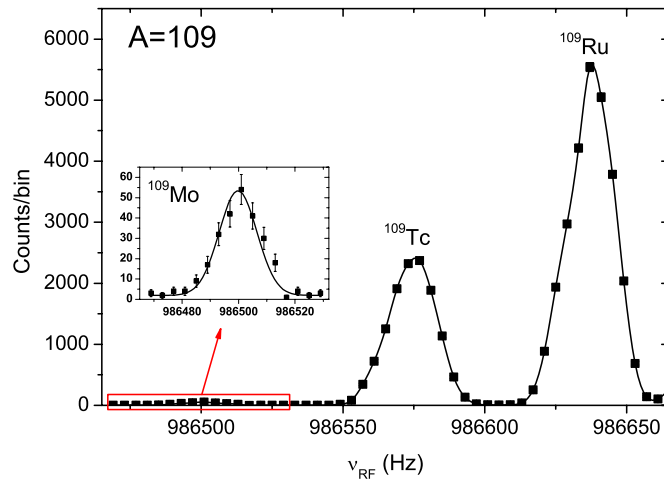
Figure 3. The number of detected ions as a function of applied frequency in the purification trap at $A = 109$. The frequency was scanned in 4 Hz steps. The inset shows the distribution for ^{109}Mo.
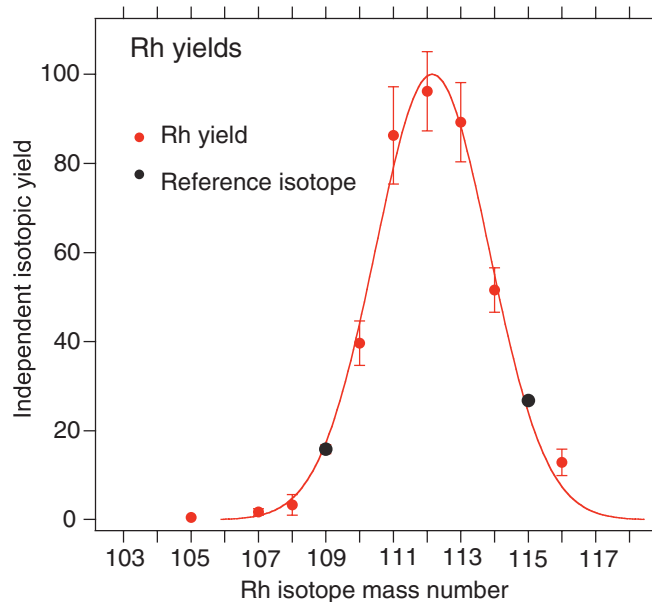

Figure 4. Independent isotopic yields of Rh isotopes. The yields are given as percentages of the height of the fitted Gaussian peak. ^{109}Rh and ^{115}Rh were used as references for the Rh isotopes. See [27] for details of yield determination.

The first trap has also been used to study independent fission yields [26, 27]. Figure 4 gives an example of isotopic yield distribution for rhodium measured at IGISOL.

Sometimes purification with the first trap leaves some unwanted ions (from an isomeric state or neighbouring isobar) to the ion bunch. With a so-called Ramsey cleaning technique [28] a mass resolving power up to $m/\Delta m \approx 10^6$ can be achieved. In that method, the purified ions from the first trap are further cleaned by applying dipolar excitation at reduced cyclotron frequency of the contaminant ion in the form of time-separated oscillatory fields [29–31] in the precision trap. This drives the unwanted species to a larger orbit but the ions of interest

stay unaffected. After the dipolar excitation, only the ions of interest can pass through the 2 mm diaphragm back to the purification trap for recooling and recentring before actual mass measurement in the precision trap. This dipolar cleaning method is useful both for mass measurements and for trap-assisted spectroscopy if the normal first trap purification is not sufficient to produce clean ion bunches.

High-precision mass measurements are performed employing the time-of-flight ion cyclotron resonance technique [32, 33] in the precision trap. There, a dipole excitation is firstly applied to ions to increase their magnetron radius. A subsequent quadrupole excitation converts the magnetron motion into a reduced cyclotron motion periodically. When the excitation frequency matches with the sideband frequency, the radial energy of the ions reaches its maximum value after one full conversion from initially pure magnetron motion to reduced cyclotron motion. The gain in radial energy is observed as a shorter time-of-flight to the microchannel plate detector when extracted from the trap in the strong magnetic field gradient.

Figure 5(a) shows a TOF spectrum for ^{134}Sb obtained by applying a continuous quadrupolar excitation of 800 ms without Ramsey-cleaning. A contribution from the isomeric state at 279(1) keV [34] is clearly seen in this spectrum. When Ramsey cleaning is applied, the ground and the isomeric state can be measured separately. If the quadrupolar excitation is applied as time-separated oscillatory fields [35, 31], e.g. as two pulses separated by a longer waiting time, the sideband minima are steeper and the resonance is narrower. As a result, the cyclotron frequency can be determined more precisely. This can be seen from the TOF resonances for the ground and the isomeric state of ^{134}Sb (figures 5(b) and (c)) for which a Ramsey-excitation pattern of 25 ms–350 ms–25 ms (on–off–on) has been applied: the resonance width is roughly similar to the 800 ms excitation and the sideband minima are much steeper. With a continuous excitation of 400 ms the line width should have been doubled from the 800 ms excitation since the width is inversely proportional to the excitation time.

The magnetic field B is calibrated with a reference ion whose mass is well-known. At JYFLTRAP, the ions have typically a charge state $q = +e$. Thus, the mass of the nuclide of interest can be determined as:

$$m_{\text{meas}} = r(m_{\text{ref}} - m_e) + m_e, \tag{2}$$

where $r = \frac{\nu_{c,\text{ref}}}{\nu_{c,\text{meas}}}$ is the cyclotron frequency ratio between the reference ion and the ion of interest, m_{ref} is the atomic mass of the reference and m_e is the electron mass.

Nowadays data acquisition is done interleavedly [36] at JYFLTRAP: after one or two frequency sweeps for the reference ion, a few frequency sweeps are collected for the ion of interest and this pattern is repeated as long as required for sufficient statistics. The files are divided into smaller parts in such a way that a proper count-rate class analysis [37] can be applied for the datasets. The interleaved scanning reduces the uncertainty due to time-dependent fluctuations in the magnetic field, which for JYFLTRAP have been determined as $\delta_B(\nu_{\text{ref}})/\nu_{\text{ref}} = 5.7(8) \times 10^{-11} \text{ min}^{-1}\Delta t$, where Δt is the time between the two reference measurements. This error is quadratically added to the statistical uncertainty of each frequency ratio. The weighted mean of the measured frequency ratios is calculated and used as the final value. The inner and outer errors [38] of the data sets are compared and the larger value of these two is taken as the error of the mean. The mass-dependent uncertainty of JYFLTRAP and remaining residual relative error have been thoroughly investigated via carbon cluster measurements [39]. The uncertainty due to mass-dependent shift $\delta_{m,\text{lim}}(r)/r = (7.5 \pm 0.4 \times 10^{-10}/u) \times \Delta m$ [39] and an additional residual relative uncertainty $\delta_{\text{res,lim}}(r)/r = 7.9 \times 10^{-9}$ [39] are quadratically added to the error. More details of the JYFLTRAP facility can be found from [16].
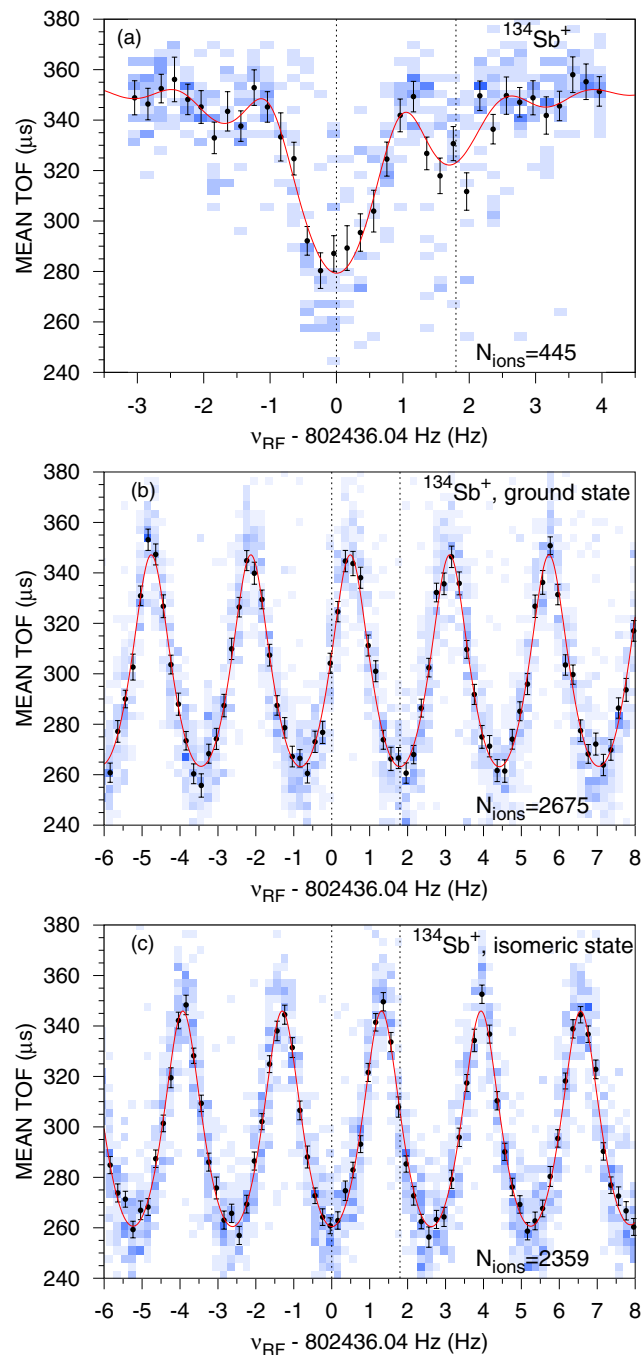
Figure 5. Time-of-flight spectra of ^{134}Sb: (a) without Ramsey cleaning and with a continuous quadrupolar RF excitation of 800 ms, (b) Ramsey-cleaned ground state with a 25–350–15 ms (on–off–on) excitation and (c) Ramsey-cleaned isomeric state with a 25–350–15 ms (on–off–on) excitation. The number of ions in a bunch has been limited to 1–2 ions/bunch and the time gate has been set to 217.6–390.4 μs in these figures. The blue squares indicate the number of ions in each time-of-flight bin: the darker the colour, the more ions there are. The dashed lines show the positions of the resonance frequencies for the ground and isomeric states.

3. Results

3.1. Overview of Penning-trap measurements

During recent years, masses of around 300 fission fragments have been measured with Penning traps. Most of the measurements have been performed at JYFLTRAP [40–50] and ISOLTRAP [51–63, 8] facilities. Some nuclei in the relevant region have also been studied at CPT [64, 65], LEBIT [66] and TITAN [23]. JYFLTRAP and ISOLTRAP provide also databases of their results [67, 68]. The list of measured ground-states is given in table 1 whereas the measured isomeric states or (possible) mixtures of states are tabulated in table 2.

Before the Penning-trap era, most of the mass values of fission fragments were based on beta-decay endpoint energies. This indirect method tend to underestimate the mass values due to unobserved feeding to higher lying excited states in the daughter nucleus (pandemonium effect [70]). Direct Penning-trap measurements have revealed large discrepancies to tabulated mass values based mainly on beta-decay energies. The effect accumulates and is more pronounced towards more neutron-rich members of an isobaric chain. The pandemonium effect is seen in figure 6 where the deviation between the Penning trap measurement of fission fragments to the Atomic Mass Evaluation 2003 (AME03) [71] values have been plotted as a function of isospin projection $T_Z = (N - Z)/2$. In general, the difference from the AME03 values largely based on beta-decay experiments is bigger for more neutron-rich nuclei (higher T_Z). Some of the earliest ISOLTRAP results have already been included in the AME03. Therefore, they deviate less from the AME03 than the other experimental results.

The dramatic influence of the Penning-trap measurements on the atomic mass evaluation is seen in figure 6. The deviations of the Penning-trap values compared to the preview of the forthcoming Atomic Mass Evaluation called here as AME11 [17] are much smaller than to the AME03 values. Most of the results have been included in the AME11 except the latest results from JYFLTRAP [48, 49] and CPT [65]. Nevertheless, the new results [48, 49, 65] deviate less from the AME11 values than the Penning-trap measurements in general from the AME03. For example, the results of [48, 49] are in agreement with the extrapolated values of AME11 when the error bars are taken into account. There are only a few cases where the Penning trap data included in the AME11 show a more than 1σ deviation to the evaluation. These are [95]Rb, [95]Y, [106]Tc and [115]Ru (JYFLTRAP), [65]Ni, [72]Ga, [91]Sr, [95]Sr, and [136,137]Cs (ISOLTRAP), [146]La and [148]Pr (CPT), and [64]Co (LEBIT). For these nuclides, the absolute deviations to AME11 are generally small the biggest deviations being around 100 keV ([64]Co, [115]Ru, [148]Pr). An isomeric state has been suggested to explain the large discrepancy for [64]Co [66]. Also [148]Pr has a long-lived isomeric state. [115]Ru should be further investigated to find out an explanation for the deviation.

Most of the Penning-trap mass measurements have been performed with JYFLTRAP and ISOLTRAP Penning traps. The IGISOL method used to produce ions for JYFLTRAP experiments is chemically insensitive but the primary beam intensity is much lower compared to ISOLDE. At ISOLTRAP, the experiments have focused on noble gases (Kr and Xe) for which a plasma ion source with a cooled transfer line is ideal, on elements for which resonant laser ionization can be applied (Ni, Cu, Zn, Ag) and on elements for which surface ionization can be exploited (Cr, Ga, Rb, Sr, Cd, Cs, Ba). At JYFLTRAP, the majority of experiments have focused on refractory elements between Y and Pd not studied elsewhere but also several isotopes from Ni to Br and from Cd to Te have been studied.

There are 19 common isotopes, mainly of Zn, Cd and Sn, investigated both at JYFLTRAP and ISOLTRAP (see figure 7). The overall agreement between ISOLTRAP and JYFLTRAP measurements is good. The only deviations occur at [123]Cd and [133]Sn. The difference for [133]Sn

Table 1. Fission products whose ground-state masses have been determined with Penning traps.

Nuclide	Ref. ion	Trap	Ref.
^{56,57}Cr	^{85}Rb$^+$	ISOLTRAP	[55]
$^{63-64}$Fe	HC$_2$F$_2^+$	LEBIT	[66]
^{65}Fe	O$_2^+$	LEBIT	[66]
^{66}Fe	SiF$_2^+$	LEBIT	[66]
^{64}Co	HC$_2$F$_2^+$	LEBIT	[66]
^{65}Co	O$_2^+$	LEBIT	[66]
^{66}Co	COF$_2^+$	LEBIT	[66]
^{67}Co	SiF$_2^+$	LEBIT	[66]
$^{65-69}$Ni	^{85}Rb$^+$	ISOLTRAP	[58]
$^{70-73}$Ni	^{72}Ge$^+$	JYFLTRAP	[44]
$^{66-74,76}$Cu	^{85}Rb$^+$	ISOLTRAP	[58]
^{73,75}Cu	^{72}Ge$^+$	JYFLTRAP	[44]
$^{72-81}$Zn	^{85}Rb$^+$	ISOLTRAP	[60]
$^{76-80}$Zn	^{88}Rb$^+$	JYFLTRAP	[46]
$^{72-78}$Ga	^{85}Rb$^+$	ISOLTRAP	[58]
$^{78-83}$Ga	^{88}Rb$^+$	JYFLTRAP	[46]
$^{80-85}$Ge	^{88}Rb$^+$	JYFLTRAP	[46]
$^{81-87}$As	^{88}Rb$^+$	JYFLTRAP	[46]
$^{84-89}$Se	^{88}Rb$^+$	JYFLTRAP	[46]
$^{85-92}$Br	^{88}Rb$^+$	JYFLTRAP	[43]
$^{88-95}$Kr	^{85}Rb$^+$	ISOLTRAP	[57]
^{96}Kr	^{85}Rb$^+$	ISOLTRAP	[62]
$^{94-97}$Rb	^{88}Rb$^+$	JYFLTRAP	[43]
^{94,97,98}Rb^{15+}	^{85}Rb^{13+}	TITAN	[23]
$^{95-100}$Sr	^{97}Zr$^+$	JYFLTRAP	[40]
$^{94,97-99}$Sr^{15+}	^{85}Rb^{13+}	TITAN	[23]
$^{95-101}$Y	^{97}Zr$^+$	JYFLTRAP	[41]
$^{102-103}$Y	^{120}Sn$^+$	JYFLTRAP	[48]
$^{98-105}$Zr	^{97}Zr$^+$	JYFLTRAP	[40]
^{100,102,104}Nb	^{97}Zr$^+$	JYFLTRAP	[45]
$^{101,103,105-107}$Nb	^{102}Ru$^+$	JYFLTRAP	[41]
^{108}Nb	^{120}Sn$^+$	JYFLTRAP	[48]
$^{102-110}$Mo	^{97}Zr$^+$	JYFLTRAP	[40]
^{111}Mo	^{111}Tc$^+$	JYFLTRAP	[48]
^{106}Tc	^{102}Ru$^+$	JYFLTRAP	[42]
$^{107-111}$Tc	^{105}Ru$^+$	JYFLTRAP	[42]
^{112}Tc	^{102}Ru$^+$	JYFLTRAP	[42]
^{113}Tc	^{129}Xe$^+$	JYFLTRAP	[48]
$^{106-112}$Ru	^{105}Ru$^+$	JYFLTRAP	[42]
^{114,115}Ru	^{120}Sn$^+$	JYFLTRAP	[48]
^{116}Ru	^{129}Xe$^+$	JYFLTRAP	[48]
$^{108,109,111,113,115,117-118}$Rh	^{120}Sn$^+$	JYFLTRAP	[42]
^{119}Rh	^{129}Xe$^+$	JYFLTRAP	[48]
$^{112-117,119}$Pd	^{120}Sn$^+$	JYFLTRAP	[42]
^{118,120}Pd	^{120}Sn$^+$	JYFLTRAP	[48]
^{121,122}Pd	^{129}Xe$^+$	JYFLTRAP	[48]
^{112,114,116,120}Ag	^{133}Cs$^+$	ISOLTRAP	[63]
^{114,120,122,124,126,128}Cd	^{133}Cs$^+$	ISOLTRAP	[63]
$^{121-128}$Cd	^{130}Xe$^+$	JYFLTRAP	[49]
^{129,131}In	^{130}Xe$^+$	JYFLTRAP	[49]
$^{127,132-134}$Sn	^{133}Cs$^+$	ISOLTRAP	[61]
^{129,130,132}Sn	^{133}Cs$^+$	ISOLTRAP	[56]
^{130,135}Sn	^{130}Xe$^+$	JYFLTRAP	[49]

Table 1. (Continued.)

Nuclide	Ref. ion	Trap	Ref.
^{131,132}Sn	^{132}Xe$^+$	JYFLTRAP	[49]
^{133,134}Sn	^{134}Xe$^+$	JYFLTRAP	[49]
$^{131-136}$Sb	^{130}Xe$^+$	JYFLTRAP	[49]
^{133}Sb	^{136}Xe$^+$	CPT	[65]
$^{132-140}$Te	^{130}Xe$^+$	JYFLTRAP	[49]
$^{134-137}$Te	^{136}Xe$^+$	CPT	[65]
$^{135,137-139}$I	^{136}Xe$^+$	CPT	[65]
$^{137-146}$Xe	^{133}Cs$^+$	ISOLTRAP	[8]
$^{137-141}$Xe	^{136}Xe$^+$	CPT	[65]
^{137}Cs	^{133}Cs$^+$	ISOLTRAP	[51, 52]
$^{138-142}$Cs	^{133}Cs$^+$	ISOLTRAP	[52]
^{141,142}Cs	^{136}Xe$^+$	CPT	[65]
$^{145-147}$Cs	^{133}Cs$^+$	ISOLTRAP	[59]
$^{139-144}$Ba	^{133}Cs$^+$	ISOLTRAP	[52]
$^{141-147}$Ba	Molecular ions	CPT	[64]
$^{143-145,147,148}$La	Molecular ions	CPT	[64]
$^{145-151}$Ce	Molecular ions	CPT	[64]
$^{149-153}$Pr	Molecular ions	CPT	[64]
^{153,155}Pr	$C_6H_4^+$, ^{80}Kr$^+$, ^{86}Kr$^+$	CPT	[65]
^{153,155,157}Nd	$C_6H_4^+$, ^{80}Kr$^+$, ^{86}Kr$^+$	CPT	[65]
$^{153,155-159}$Pm	$C_6H_4^+$, ^{80}Kr$^+$, ^{86}Kr$^+$	CPT	[65]
$^{155,157-161}$Sm	$C_6H_4^+$, ^{80}Kr$^+$, ^{86}Kr$^+$	CPT	[65]
$^{158-161}$Eu	$C_6H_4^+$, ^{80}Kr$^+$, ^{86}Kr$^+$	CPT	[65]
^{163}Gd	$C_6H_4^+$, ^{80}Kr$^+$, ^{86}Kr$^+$	CPT	[65]

is close to 1σ and can be explained by statistics (the probability to lie beyond the 1σ band is around 32%). The discrepancy at ^{123}Cd is most likely due to the $11/2^-$ isomer in ^{123}Cd. At JYFLTRAP, both the ground and the isomeric state of ^{123}Cd have been measured [49, 50] and found to agree with earlier beta-decay experiments and disagree with the previously deduced excitation energy for the isomer. The ISOLTRAP value not corrected by the possible isomer contribution is above the mass-excess value measured for the isomeric state at JYFLTRAP. Thus, ISOLTRAP has most likely measured the $11/2^-$ isomer although the value is higher than measured for the isomeric state at JYFLTRAP.

At CPT, a combination of a strong ^{252}Cf source and a gas catcher has been employed and the measurements have focused on heavier isotopes from Sb to Gd [64, 65]. Six antimony and tellurium isotopes have been measured both at CPT and JYFLTRAP (see figure 8). In general, the results agree with each other. The deviation at ^{137}Te is rather small (1.3σ) and the discrepancy at ^{134}Sb can be explained if the isomeric state ^{134}Sb^m has been measured at CPT. The agreement between the ISOLTRAP and CPT results is also good (see figure 9). Of the 11 nuclides measured both at CPT and ISOLTRAP, the only significant deviation is found at ^{138}Xe (1.7σ).

3.2. Isomeric states

Many fission fragments have long-lived excited states, isomers, which have to be taken into account in Penning-trap mass measurements. Very short-lived isomers ($T_{1/2} \ll 100$ ms) do not disturb the experiments. Isomers with excitation energies of more than around 100 keV can be resolved from the ground state. More than 20 isomers of fission fragments have been

Table 2. Fission products for which an isomeric state (m or n) has been determined with a Penning trap or the measured state is a mixture of states or remains unknown (x).

Nuclide	Ref. ion	Trap	Ref.
^{65}F^m	O_2^+	LEBIT	[66]
^{67}Co^m	SiF_2^+	LEBIT	[66]
^{68}Cu^m	^{85}Rb$^+$	ISOLTRAP	[69, 58]
^{70}Cu^m, ^{70}Cu^n	^{85}Rb$^+$	ISOLTRAP	[54, 58]
^{71}Zn^m	^{85}Rb$^+$	ISOLTRAP	[60]
^{82}As^m	^{88}Rb$^+$	JYFLTRAP	[46]
^{90}Rb^m	^{85}Rb$^+$	ISOLTRAP	[53]
^{96}Y^m	^{97}Zr$^+$	JYFLTRAP	[41]
^{97}Y^m	^{97}Zr$^+$	JYFLTRAP	[41]
^{100}Y^m	^{97}Zr$^+$	JYFLTRAP	[41]
^{100}Nb^m	^{97}Zr$^+$	JYFLTRAP	[45]
^{102}Nb^m	^{102}Nb$^+$	JYFLTRAP	[45]
^{114}Tc^x	^{114}Ru$^+$	JYFLTRAP	[48]
^{113}Ru^x	^{105}Ru$^+$	JYFLTRAP	[42]
^{108}Rh^m	^{120}Sn$^+$	JYFLTRAP	[42]
^{110,112,114,116}Rh^x	^{120}Sn$^+$	JYFLTRAP	[42]
^{115}Pd^m	^{120}Sn$^+$	JYFLTRAP	[42]
^{115,117}Ag^x	^{133}Cs$^+$	ISOLTRAP	[63]
^{118}Ag^m	^{133}Cs$^+$	ISOLTRAP	[63]
$^{119,121-124}$Ag^x	^{133}Cs$^+$	ISOLTRAP	[63]
^{123}Cd^m	^{133}Cs$^+$	ISOLTRAP	[63]
^{121,123,125}Cd^m	^{130}Xe$^+$	JYFLTRAP	[50]
^{129,131}In^m	^{130}Xe$^+$	JYFLTRAP	[50]
^{130}Sn^m	^{133}Cs$^+$	ISOLTRAP	[56]
^{130}Sn^m	^{130}Xe$^+$	JYFLTRAP	[50]
^{131}Sn^x	^{133}Cs$^+$	ISOLTRAP	[56, 61]
^{131}Sn^x	^{130}Xe$^+$	JYFLTRAP	[50]
^{134}Sb^m	^{130}Xe$^+$	JYFLTRAP	[50]
^{134}Sb^x	^{136}Xe$^+$	CPT	[65]
^{133}Te^m	^{130}Xe$^+$	JYFLTRAP	[50]
^{136}I^x	^{136}Xe$^+$	CPT	[65]
^{146}La^x	Molecular ions	CPT	[64]
^{148}Pr^x	Molecular ions	CPT	[64]

measured with JYFLTRAP and ISOLTRAP. Figure 10 shows the mass-excess values for the measured isomers compared to the NUBASE 2003 evaluation [72]. The large deviations can be mainly explained by the uncertainties related to beta-decay experiments which tend to underestimate the mass-excess values, as was shown already in figure 6. The NUBASE data for ^{82}As^m, ^{96}Y^m, ^{97}Y^m, ^{108}Rh^m, ^{125}Cd^m, ^{129}In^m, ^{131}In^m and ^{134}Sb^m, from which the JYFLTRAP measurements differ most, are based on beta-decay energies. For ^{97}Y, the ground-state is based on beta-decay energy. For ^{123}Cd^m, the NUBASE value is also based on beta-decay experiments but there, some of the beta-gates used to determine the ground-state endpoint energy belonged to the isomeric state [50]. This has led to an overestimation of the ground-state mass value in NUBASE.

For many nuclides, both the ground and the isomeric state of a nucleus have been measured with a Penning trap and the excitation energy has been determined. Figure 11 shows the excitation energies of the isomers compared to the NUBASE values. For ^{71}Zn, ^{90}Rb, ^{97}Y and ^{118}Ag, the ground-state has not been measured with a trap and the value has been adopted
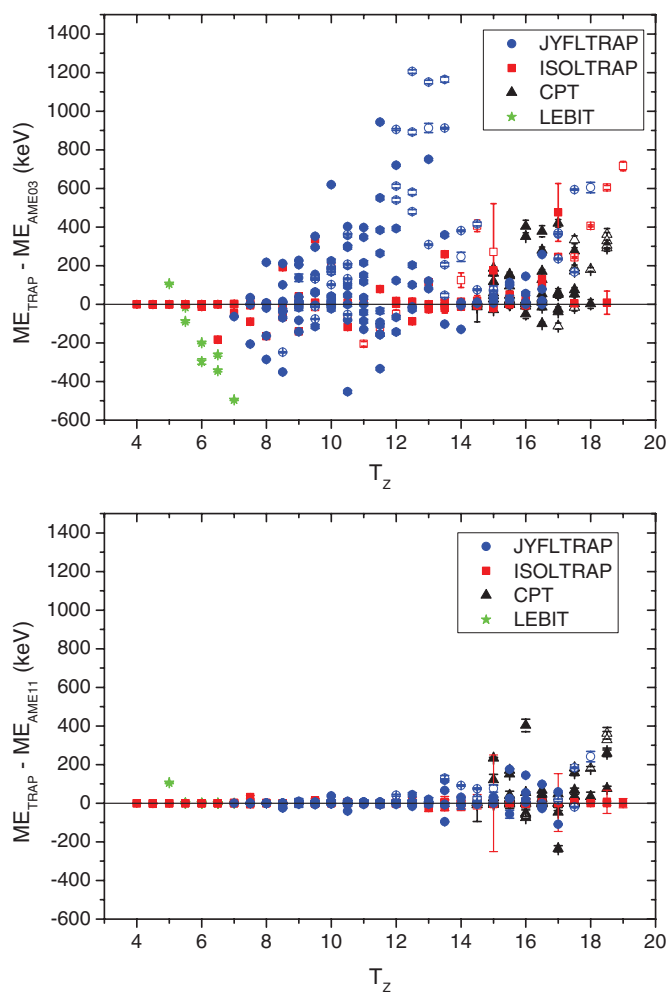
Figure 6. Penning trap measurements of neutron-rich nuclei in the relevant fission region and comparison to the AME03 [71] (top) and 2011 [17] (bottom). The error bars show the uncertainties related to the trap measurements only. Open symbols denote that the corresponding AME values are based on extrapolations. A part of the ISOLTRAP data has already been included in the AME03. The JYFLTRAP values deviating from the AME11 are mainly based on data not included in the AME11 [48, 49].

from the AME11. Large discrepancies are observed for ^{96}Y^m, ^{100}Nb^m, ^{108}Rh^m, ^{125}Cd^m, ^{129}In^m, ^{131}In^m and ^{134}Sb^m whose NUBASE values are based on beta-energy differences. Penning traps offer a new and more accurate method to measure excitation energies for beta-decaying isomers in particular.

In many cases, the measured state cannot be assigned to the ground or to the isomeric state. Examples are ^{114}Tc, ^{113}Ru, ^{110,112,114,116}Rh, ^{115,117,119,121,122,123,124}Ag and ^{131}Sn. If the excitation energy is too low to be separated from the ground state, a correction to the measured value has to be made. There, the production ratio of the states is crucial and a simple assumption of 1:1 production ratio may lead to inaccurate mass values. In future, post-trap spectroscopy should be employed to identify the measured state.
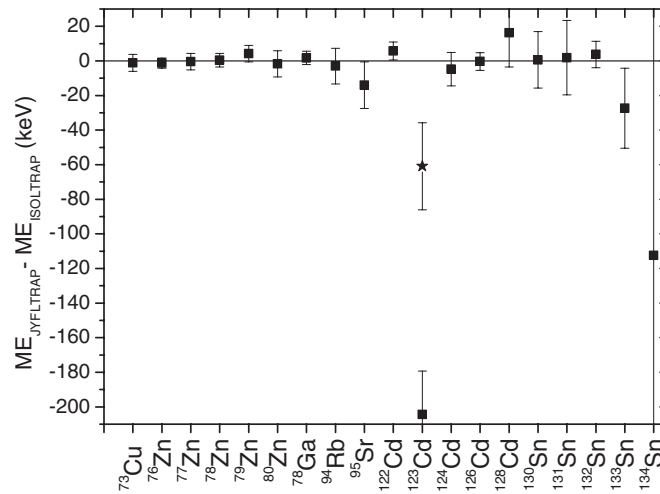
Figure 7. Comparison of JYFLTRAP [40, 43, 44, 46, 49] and ISOLTRAP [58, 60, 53, 63, 56, 61] data. The star denotes the deviation to the isomeric state measured at JYFLTRAP. The ISOLTRAP value for ^{123}Cd is the measured value without corrections due to a possible mixture of states.
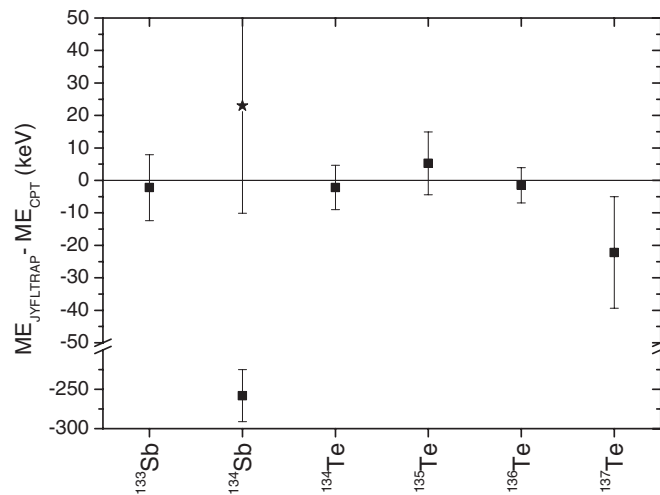

Figure 8. Comparison of JYFLTRAP [49] and CPT data [65]. The star denotes the deviation to the mass excess value of ^{134}Sb^m measured at JYFLTRAP. Note the difference in vertical scale before and after the axis break.

4. Discussion

4.1. Comparison to different mass models

We compared the masses of the fission fragments measured with Penning traps to different mass models. Three selected models that gave the best agreement were the Finite Range Droplet Model (FRDM95 [73]), which is a microscopic–macroscopic model applying shell model corrections onto liquid-drop model, the model by Duflo and Zuker [74], which separates the Hamiltonian into monopole and multipole terms, and a mean-field model HFB-21 [75].
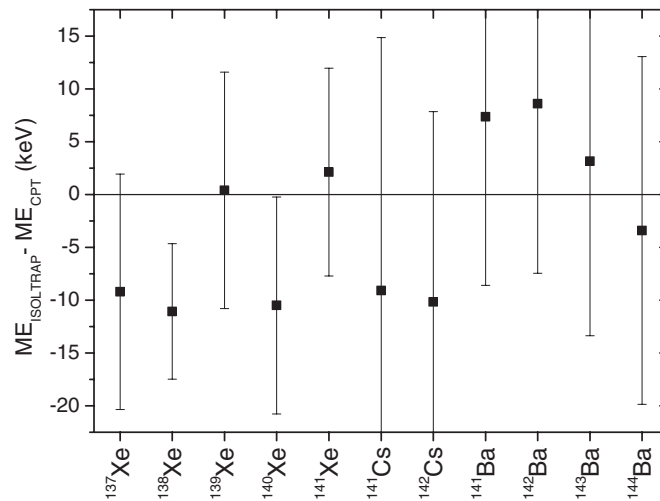
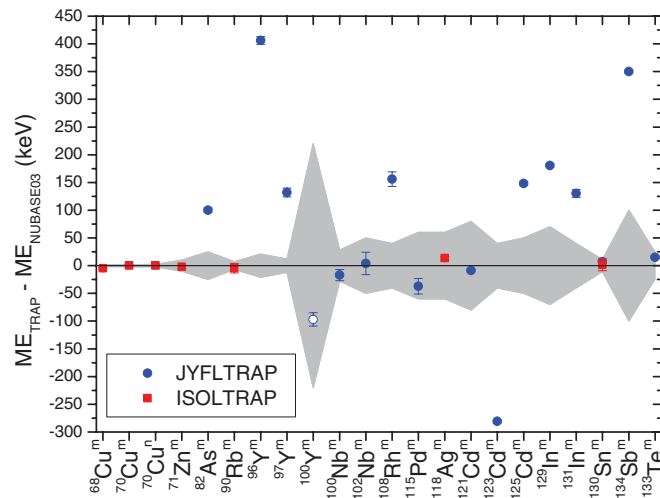**Figure 9.** Comparison of ISOLTRAP [52, 8] and CPT data [64, 65].

Figure 10. Mass excess values for the isomeric states measured with JYFLTRAP or ISOLTRAP and comparison to the NUBASE 2003 [72] values. The grey band shows the uncertainties related to the NUBASE 2003 values.

The updated mass values had the biggest impact on the root-mean-square deviation (σ_{rms}) of the model HFB-21, which was decreased by around 100 keV compared to the dataset based on AME03 values. For the used dataset, the model Duflo–Zuker has the lowest rms deviation. Whereas the comparison of the new experimental data to AME03 revealed larger deviations for more neutron-rich nuclei, the trend is relatively flat for FRDM, Duflo–Zuker and HFB-21 (see figure 12).

Three models based on energy density functionals were also compared to our dataset: SLy4 [76, 77], SkP [76, 77] and a model based on the generator coordinate method (GCM) employing the Sly4 energy density functional in the deformed basis with dynamical quadrupole
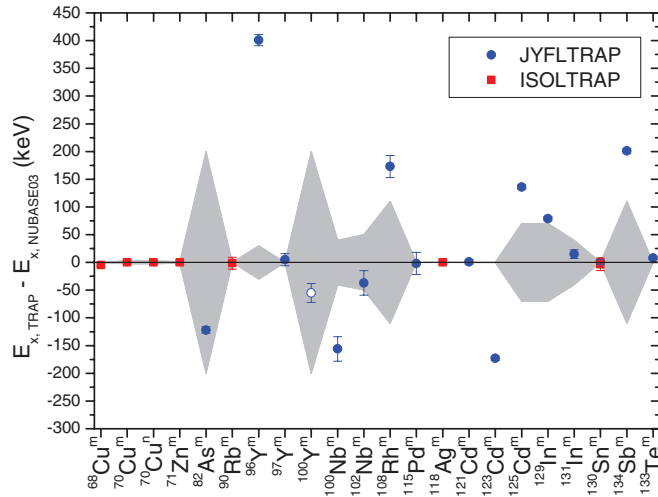
Figure 11. The excitation energies of the isomers measured with JYFLTRAP or ISOLTRAP and comparison to the NUBASE 2003 [72] values. The grey band shows the uncertainties related to the NUBASE 2003 values.

correlations (GCM J=0) [3]. Typical rms deviations of these functionals have been around 3.14 MeV (SkP) [78], 5.10 MeV (SLy4) [78] and 5.33 MeV (GCM) [3]. For the dataset used here, the rms deviations are around $2 - 3$ MeV for these models. There is a clear trend when moving towards higher T_Z nuclei: the model values increase more than the experimental data (see figure 13). The GCM (J=0) and SkP models show the largest deviations to experimental data at low T_Z whereas the model SLy4 gives the worst predictions for the most neutron-rich nuclei. Both the GCM (J=0) and SkP models underestimate the masses by around $1 - 2$ MeV whereas SLy4 overestimates the mass values by around 2 MeV. The results do not change much when the updated mass values are used instead of AME03.

4.2. Two-nucleon binding energies

The study of the evolution and interplay of shell structure and collective properties as a function of proton and neutron numbers requires accurate knowledge of the fine structure of the mass surface. The fine structure is best viewed in the systematic evaluation of mass differentials as a function of proton and neutron number. Typical mass differentials are one- and two-nucleon separation energies and decay Q-values. A similar request holds for second order differentials such as the shell gap energies and odd–even staggering (OES) of masses related to pairing effects. With the present-day ion-trap spectrometry these quantities are typically available with accuracies of the order of 10 keV or better. This offers accuracy comparable to that of excited states spectroscopy far from stability in the outskirts of the known nuclear landscape.

The two-neutron separation energy S_{2n} can be obtained by using the following formulae:

$$S_{2n} = E(A, Z) - E(A - 2, Z) = [M(A - 2, Z) + 2M_n - M(A, Z)]c^2, \quad (3)$$

where E and Mc^2 stand for the binding energy and mass, respectively. Two-proton separation energies are determined analogously. In the following sections, two-nucleon binding energies of neutron-rich nuclei are presented in a few selected regions. Firstly, the behaviour of S_{2n} values between the closed shells in the deformed region around $N = 60$ and at subshell closure
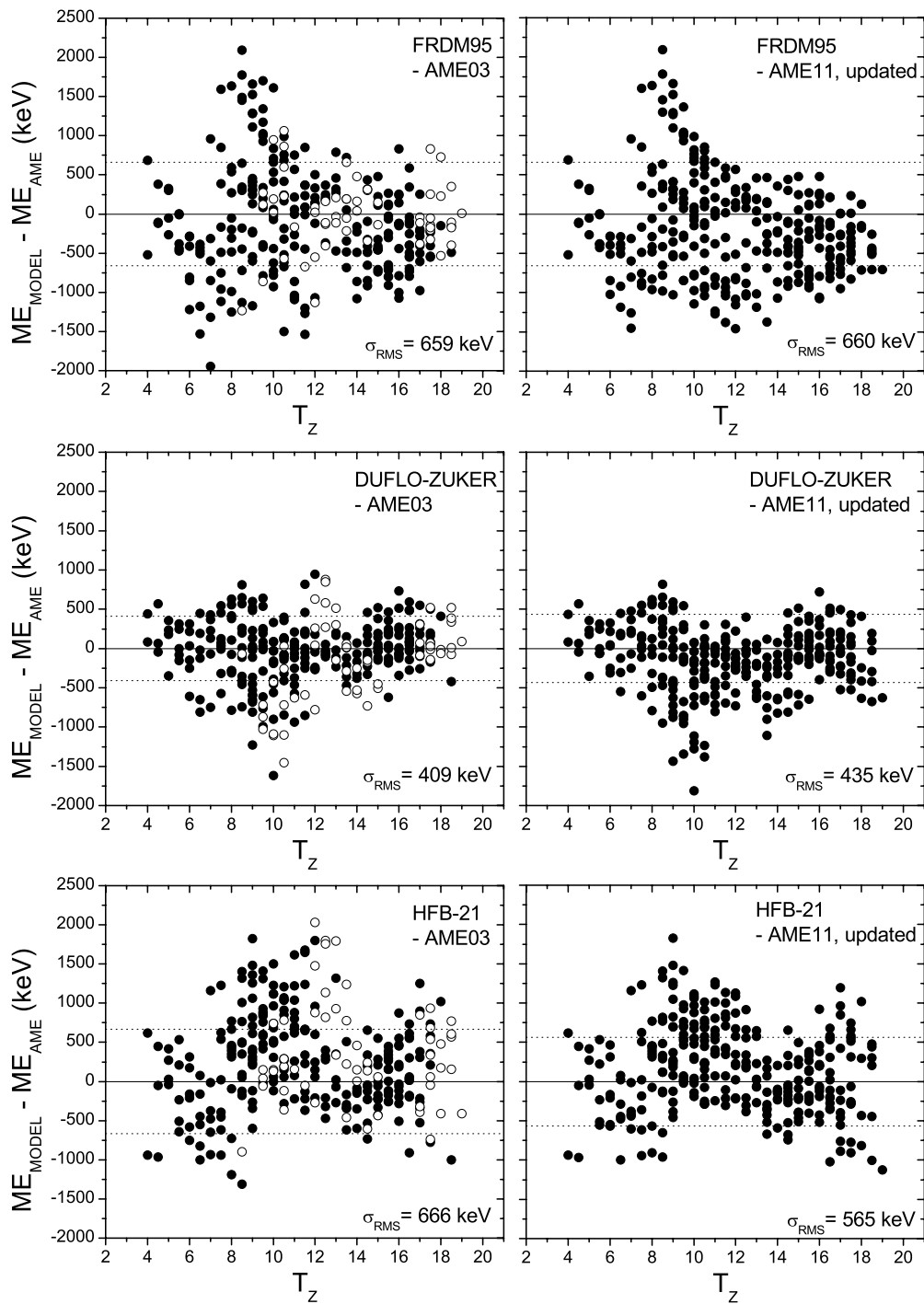
Figure 12. Differences between experimental and theoretical mass excess values as a function of isospin projection T_Z for models FRDM95 [73], Duflo–Zuker [74] and HFB-21 [75]. The dashed lines show $1\sigma_{rms}$ deviations from zero.
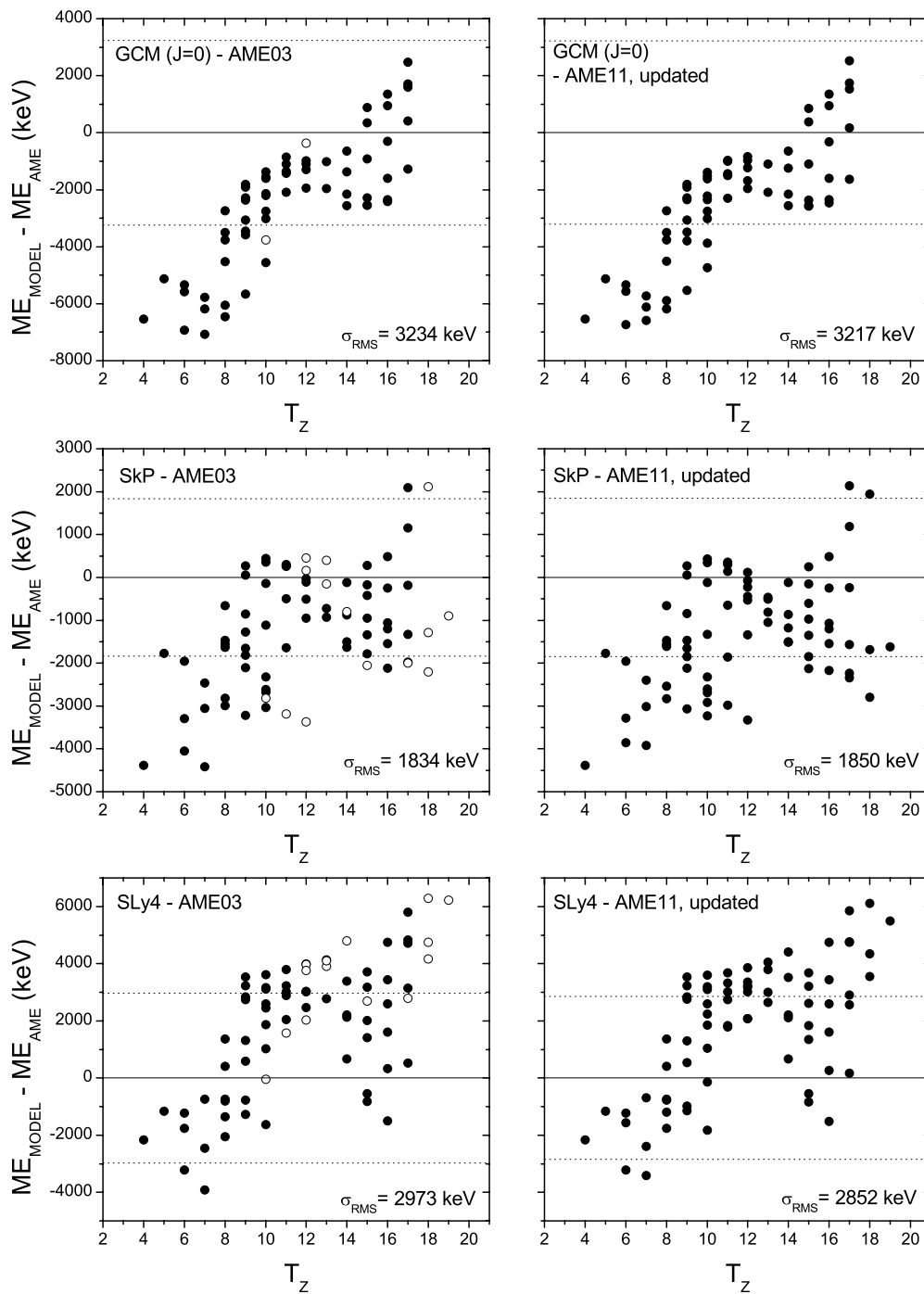
Figure 13. Differences between experimental and theoretical mass excess values as a function of isospin projection T_Z for models GCM (J=0) [3], SkP [76, 77] and SLy4 [76, 77]. The dashed lines show $1\sigma_{rms}$ deviations from zero.
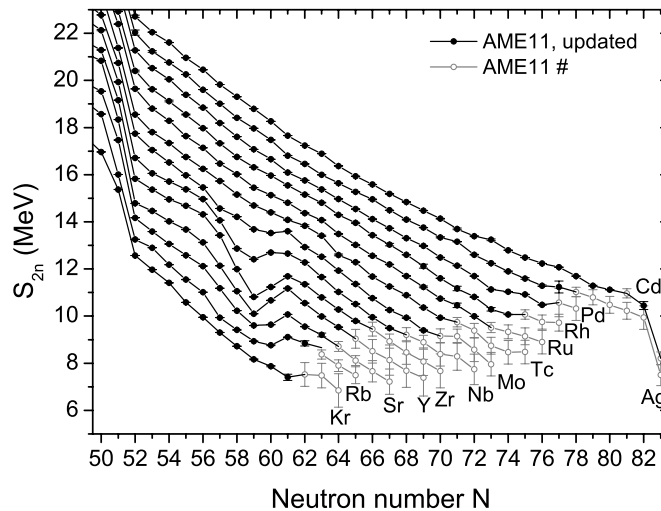
Figure 14. Two-neutron binding energy as a function of neutron number from Kr ($Z = 36$) to Cd ($Z = 48$).

at $N = 40$ are discussed. Then, shell closures at $N = 50$, $Z = 28$, $Z = 50$, and $N = 82$ are reviewed.

4.2.1. Shape transitions at $N \approx 60$. Neutron-rich nuclei between $N = 50$ and 82 display a rich landscape of changing structures influencing the mass-energy surface in a dramatic way. In particular, the neutron-rich isotopes around $A = 100$ have been investigated for a shape transition and coexistence of shapes around $Z = 40$ and $N = 60$, see [79] and references therein. While the ground states of the strontium and zirconium isotopes below $N \approx 60$ appear to be only weakly deformed or nearly spherical, the heavier isotopes display mainly axially symmetric deformed shapes. In 1994 spectroscopic studies of Lhersonneau *et al* [80] showed that nuclei with $N > 60$ have large ground state quadrupole deformations, while the intermediate $N = 59$ isotones of strontium, yttrium and zirconium still have nearly spherical ground states. This interpretation has since then been confirmed by a series of collinear laser spectroscopy experiments in the form of a sudden increase of the mean-square charge radii around $N = 60$ [81]. When moving towards higher Z, molybdenum isotopes are, however, found to be already less deformed or even posses triaxial shapes. Two-neutron separation energies shown in figure 14 highlight the influence of strong ground state deformation on masses as a deep dip below $N = 61$ which corresponds to a distinct local maximum in two-neutron binding. The behaviour of charge radii together with two-neutron binding energies is shown in figure 15.

In their recent theoretical paper Takahara *et al* [82] showed that the spin–orbit potential plays a decisive role in the predominance of prolate deformation of ground states. This is also the case for neutron-rich nuclei above $N = 60$ where neutrons start to occupy deformed orbits deriving from the $g_{7/2}$ having considerable overlap with the spin–orbit partner proton orbits deriving from the $g_{9/2}$ single-particle level. The correlation between the relevant neutron and proton orbits drives the nucleus to large deformations for nuclides with $Z = 38 - 41$ and $N > 60$. This picture is also supported by the recent mass measurements of neutron-rich Kr
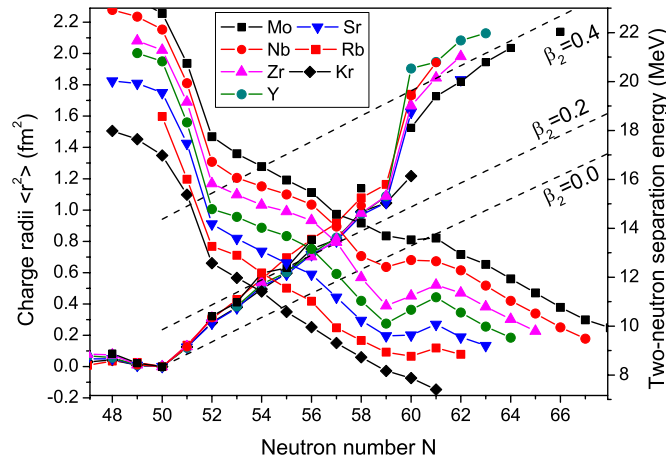
Figure 15. Two-neutron binding energies and differences in mean-square charge radii around $N = 60$. Charge radii differences of each isotope chain are given relative to the charge radii of the $N = 50$ isotope.
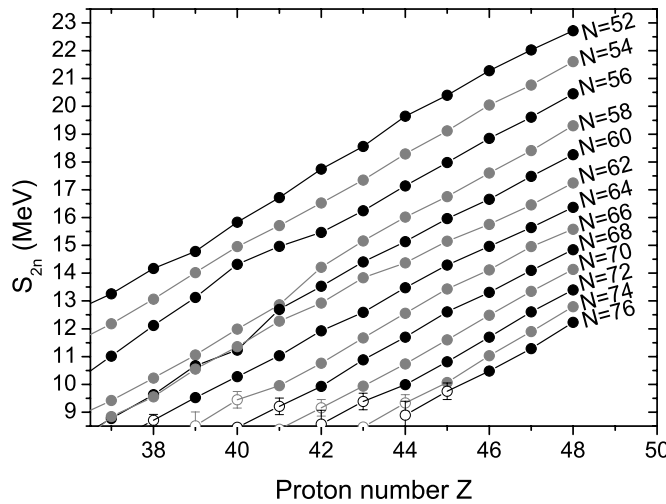

Figure 16. Two-neutron separation energies as a function of proton number for even-N isotonic chains around deformed shell closure at $N = 59$. The open symbols are based on extrapolated mass values [17].

isotopes ($Z = 36$) [62] where protons are not yet occupying the $g_{9/2}$ orbit resulting in a nearly monotonically decreasing trend in S_{2n}.

Local maxima in two-nucleon separation energy curves can be related to energy gaps due to shell stabilization effects. In order to probe the existence of such gaps one can plot S_{2n} values for isotones as function of the proton number as shown in figure 16 for neutron-rich nuclei studied with the JYFLTRAP. A distinct energy gap is observed when crossing the $N = 58$ neutron number which coincides with the onset of deformation. For Zr, one observes even a crossing of the curves corresponding to $N = 60$ and 62. Otherwise, the curves show a smooth nearly monotonic behaviour indicating only weak structural effects over a broad range of proton and neutron numbers.
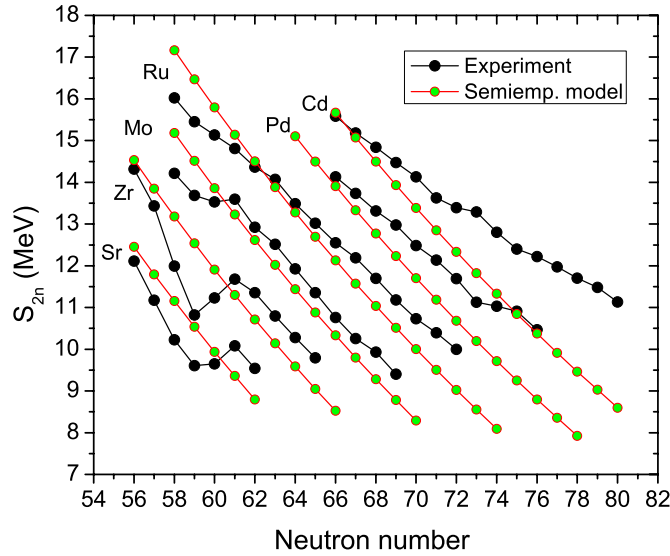
Figure 17. Two-neutron separation energies for even-Z isotopes as a function of neutron number in comparison with semiempirical liquid drop model (see [85]).

For nuclei with larger proton and or neutron numbers, the situation becomes more complex with the mixing of many configurations and less pronounced axial deformation. Two-neutron separation energies show behaviour which signals either their non-sensitivity to structural changes or appearance of weak structural changes in the ground states. It is tempting to view the values compared to a simple liquid drop model approach based on the semiempirical mass formula [83, 84]. Using the formula for two-neutron separation energy and the coefficients from [85] two-neutron separation energies for neutron-rich Zr, Mo, Ru, Pd and Cd isotopes were calculated and are plotted with the experimental values in figure 17. Except for the discontinuities around $N = 60$, the overall trend in the slopes for Zr and Mo isotope chains is produced. However, when moving towards higher-Z isotope chains and $N = 82$ neutron number, an increasing shift in the trends of S_{2n} energies as compared to the droplet model is seen. It is obvious that a more refined theoretical approach is needed.

The mean-field calculations presented in [48] provide a reasonable starting point to describe the underlying structural evolution accounting for the systematics of S_{2n}. In particular, both Gogny-D1S and Gogny-D1N energy density functionals predict a very similar evolution of the ground-state shapes as a function of the neutron number for a given isotopic chain. The agreement between the experiment and the theory is rather good in the D1S calculation, in particular for Ru and Pd isotopes. The calculation predicts appearance of a new discontinuity beyond $N = 72$ for Ru, Mo and Zr isotopes along the change of structure towards spherical shape. This would be a challenging task for future experiments to confirm or not.

Nevertheless, a close inspection of the potential energy surfaces reveals the presence of several low-lying competing configurations for the considered nuclei as well as γ-softness. This already indicates that correlations beyond the static mean-field picture, i.e. symmetry restoration and/or configuration mixing [86, 87], may play a role in the description of the considered nuclei.

4.2.2. Sub-shell closure at $N = 40$. Two-neutron separation energies are shown as a function of the neutron number in figure 18 for $Z = 25-36$. The impact of direct mass measurements by
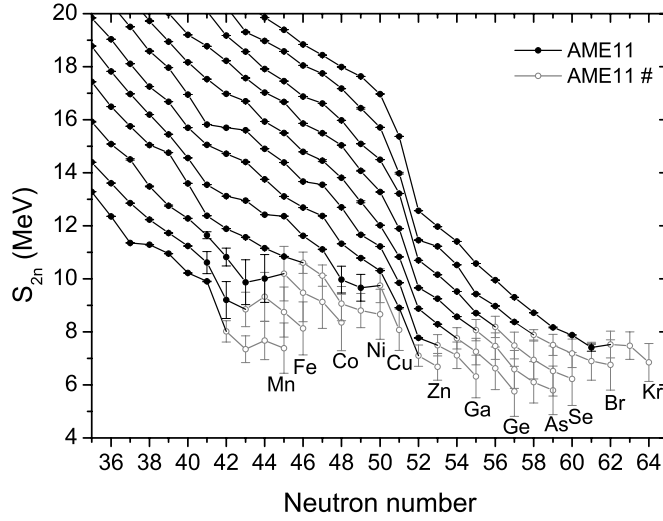
Figure 18. Two-neutron binding energy as a function of neutron number from Mn ($Z = 25$) to Kr ($Z = 36$).

Penning traps on the landscape of masses in this region is important. Generally, S_{2n} decreases smoothly with neutron number and shell effects appear as a discontinuity, most visibly at the $N = 50$ shell closure for neutrons. Smaller effects as discontinuities from a smooth trend are observed as an increased binding for $^{67}Ni_{39}$ and $^{68}Ni_{40}$. These small deviations coincide with the earlier proposed spherical sub-shell closure at $N = 40$ observed in various spectroscopic studies, although being a rather small effect compared to major shell closures of the doubly magic nuclei. However, recent measurement of g factors and quadrupole moments of the odd-A Cu isotopes support an apparent magic behaviour at $N = 40$. According to this study the effect is related to the parity change between the pf-shell orbits and the $g_{9/2}$ level. Therefore, this magic behaviour cannot be interpreted only in terms of the energy gap at $N = 40$ [88].

Moreover, a well-established change of the slope above $N = 40$ is observed for Ni and Cu isotopic chains in figure 18. This change could be due to the action of a tensor force [89]. Filling more neutrons in the $1g_{9/2}$ orbit results in the pulling-down of the orbit. In addition, with more neutrons occupying the $1g_{9/2}$ orbit the $1f_{5/2}$ and $2p_{3/2}$ orbits are crossing each other above $N = 40$. The result of these two effects will increase the S_{2n} energies and results in a reduced slope beyond $N = 40$. A similar explanation has been given for neutron-rich Ga isotopes above ^{71}Ga [90].

4.2.3. Shell closure at $N = 50$. For quantitative insight into the question of the change of masses around shell closures, one can study the two-nucleon gaps for neutrons or protons. For this purpose, we have plotted in figure 19 two-neutron separation energies for $N = 46, 48, 50, 52, 54$ and 56 isotones as a function of the proton number with the latest mass values. The energy difference between the $N = 50$ and 52 isotones corresponds to a two-neutron shell gap across $N = 50$. When moving down in Z from the semi doubly magic ^{90}Zr there is an obvious trend for lowering the value having a minimum at Ge ($Z = 32$). This corresponds also to a minimum in the systematics of the first 2^+ energies of known even-A $N = 50$ isotones suggesting maximum impact from core polarization effects. The isotone curves also indicate that the gap at $N = 50$ opens up towards the doubly magic Ni core ($Z = 28$). For magic nuclei
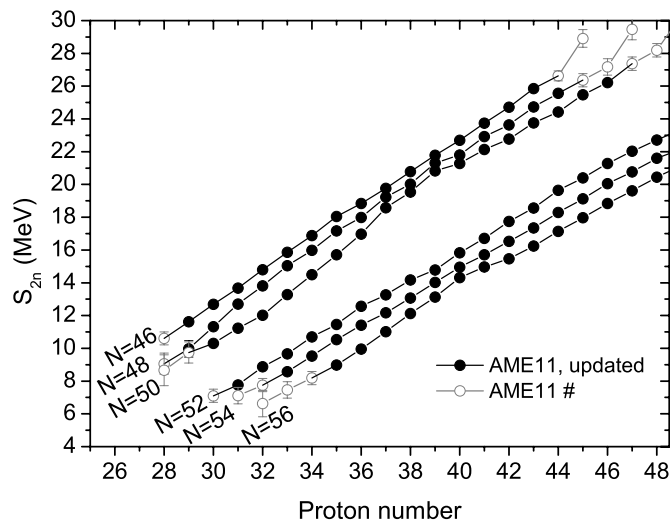
Figure 19. Two-neutron separation energy as a function of proton number for the $N = 50$ shell gap [17]. Experimental values are denoted by solid circles whereas extrapolated or at least partly extrapolated values are plotted with open circles.

the two-nucleon gap energy is approximately twice the gap of the single-particle spectrum providing a signature for the magicity [3].

Beyond the energy difference of $N = 50$ and $N = 52$ isotones, it is of interest to notice that the otherwise smooth trend of S_{2n} values for each isotone is broken for the $N = 48$ and 50 isotones between $Z = 32$ and 36. This may arise from two-particle and two-hole excitations across the shell gap. Otherwise, a rather flat behaviour indicating smoothness in energies of the $g_{9/2}$ and $d_{5/2}$ (or $s_{1/2}$) neutron states across the entire range of the studied proton numbers is observed.

In [46], experimental $N = 50$ shell gap energies were compared with two spherical mean-field calculations by Otsuka *et al* [91, 92] employing a D1S or a GT3 tensor interaction as well as three different self-consistent mean field calculations in the frame of the density functional theory [3, 77, 76] were used to calculate the $N = 50$ shell gap energies. Both calculations of Otsuka overpredicted the gap by at least a factor of 2 over the experimentally known range. The use of the tensor-based interaction brought the gap clearly down to ^{78}Ni. The two calculations of Stoitsov *et al* with Sly4 energy density functionals [76, 77] agreed in trends but differed in magnitude rather strongly depending on the inclusion of correlations. It is remarkable that the models based on the density functional theory reproduced qualitatively the trend in experimental values: a monotonic reduction from $Z = 40$ down and a minimum at $Z = 32$. They also predicted the increase in the gap energy and therefore the strengthening of the magicity towards ^{78}Ni in compliance with the concept of mutual support of magicities [93].

Figure 20 shows the experimental two-neutron gap energies for $N = 50$ in comparison with a few selected theoretical models in the region around $Z = 28 - 40$. The evolution of the shell gap over a broader range of proton numbers is shown in figure 25. The nuclear shell model clearly overpredicts the gap energies and yields a rather flat trend in shell-gap energies. The HFB Gogny with correlations [94] shows also a relatively flat trend in the gap energies and underestimates them, particularly closer to stability. The energy density functional in the
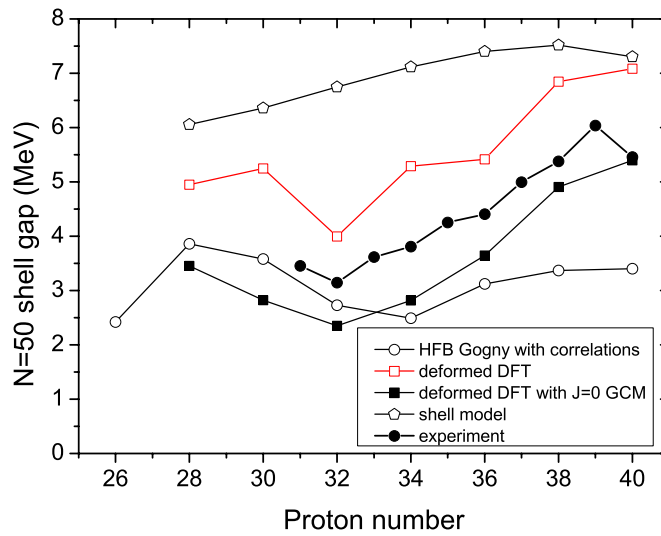
Figure 20. Evolution of the $N = 50$ shell based on most recent experimental values compared with selected theoretical models. See text for explanation of the models.
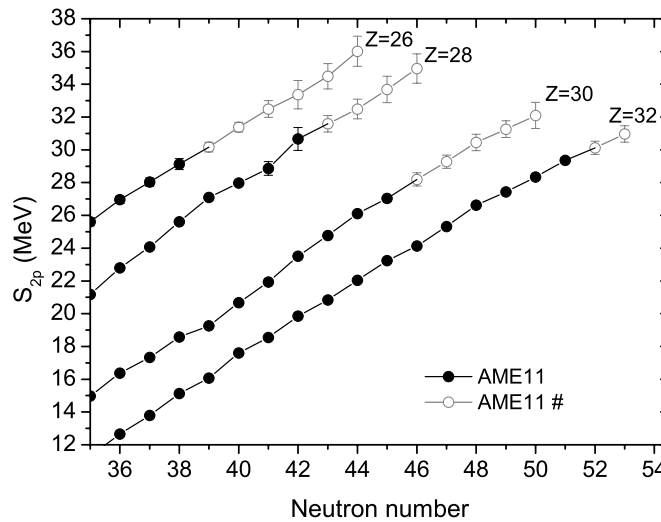

Figure 21. Two-proton separation energies S_{2p} [17] as a function of the neutron number for $Z = 26$, 28, 30 and 32 isotopic chains.

deformed basis [3] produces the trend well but gives systematically too high values for the gap energies. A similar calculation employing the SLy4 interaction in the deformed basis and adding dynamical quadrupole correlations [3] brings the calculated values closer to those observed experimentally.

4.2.4. Shell closure at $Z = 28$.   Figure 21 displays two-proton separation energies for $Z = 26$, 28, 30 and 32 isotopic chains as a function of neutron number. The $Z = 28$ shell gap energy
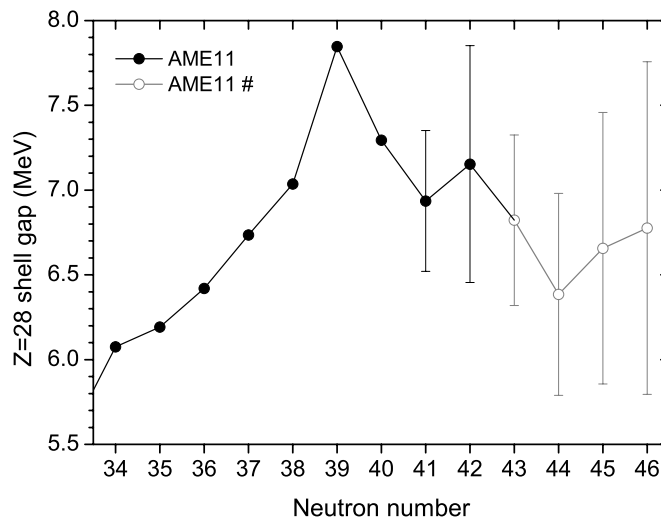
Figure 22. The evolution of the $Z = 28$ shell gap energy as a function of neutron number.

defined as a difference between the S_{2p} values of the $Z = 28$ and $Z = 30$ isotopic chains increases up to $N = 39$ after which it starts to decrease (see figure 22). The reduction in the shell gap energy has been explained by tensor force calculations [89, 91]. As more neutrons are occupying $1g_{9/2}$ orbit, $1f_{7/2}$ and $1f_{5/2}$ orbits are coming closer to each other resulting in a reduction of the proton shell gap energy at $Z = 28$ from $N = 40$ to $N = 50$. In order to understand the experimental data of copper isotopes and the decrease in the shell gap energies, it was shown in [95] that proton core excitations play an important role when approaching $N = 50$. As these theoretical calculations suggest that the $Z = 28$ shell gap becomes rather small at $N = 50$, more experimental data are required to determine the trend in experimental shell gap energies closer to $N = 50$.

4.2.5. The $Z = 50$ and $N = 82$ shell closures. The shell closure at $Z = 50$ and $N = 82$ has long been known to exhibit features of exceptional purity for its spherical single particle structure [96, 97]. This has been the result of intensive explorations by nuclear spectroscopy of excited states in this region. However, only recently the precise direct measurements of masses have become available and extended the knowledge of the ground state binding energies beyond $N = 82$ for Sn and above. The most recent results coming from JYFLTRAP and ISOLTRAP cover the masses of isotopic chains up to ^{135}Sn, ^{136}Sb, ^{140}Te and ^{146}Xe. In addition, the Penning trap mass measurements at ISOLTRAP and CPT cover heavier fission products from Cs up to Gd. All available data are summarized in the two-neutron separation energy plot shown in figure 23. A rather smooth trend is observed for all curves except when crossing the $N = 82$ shell closure. A distinct drop in binding energy is observed signalling a large and nearly constant drop in energy between $N = 82$ and $N = 84$. Beyond $N = 84$, the trends are again smooth until the deformed rare earth region around $N = 90$ is reached. Here, for the Pr isotopes a similar but less dramatic jump in S_{2n} is observed as compared to the $N = 60$ region (see figure 14).

To investigate in more details the evolution of the shell structure two-neutron separation energies are plotted as a function of proton number in figure 24. The $N = 82$ and 84 isotonic chains are separated by a large energy gap with a maximum value of about 6.5 MeV at
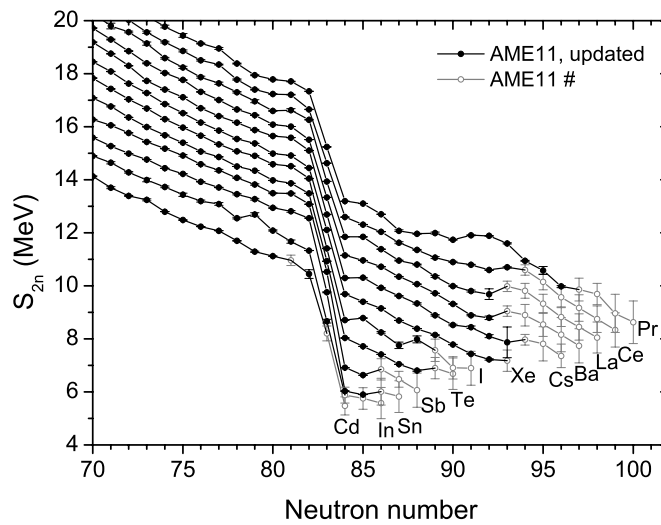
Figure 23. Two-neutron binding energy as a function of neutron number from Cd ($Z = 48$) to Pr ($Z = 59$).
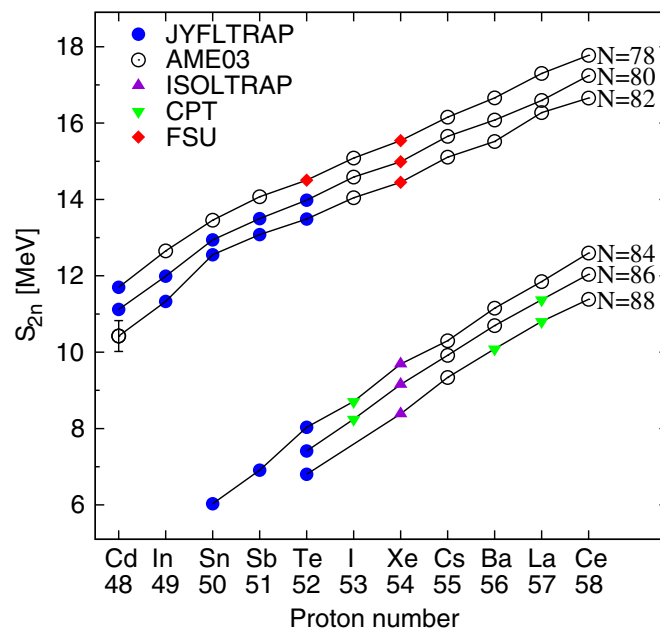
Figure 24. Two-neutron separation energy as a function of proton number for the $N = 82$ shell gap.

$Z = 50$. Outside the gap, only small separations are observed between the even-N chains. The value of the energy gap is slowly decreasing with the increasing proton number indicating the importance of correlations induced by collective effects. The dependence of the shell gap energy $\Delta = S_{2n}(N = 82) - S_{2n}(N = 84)$ on the proton number given in figure 25 indicates the
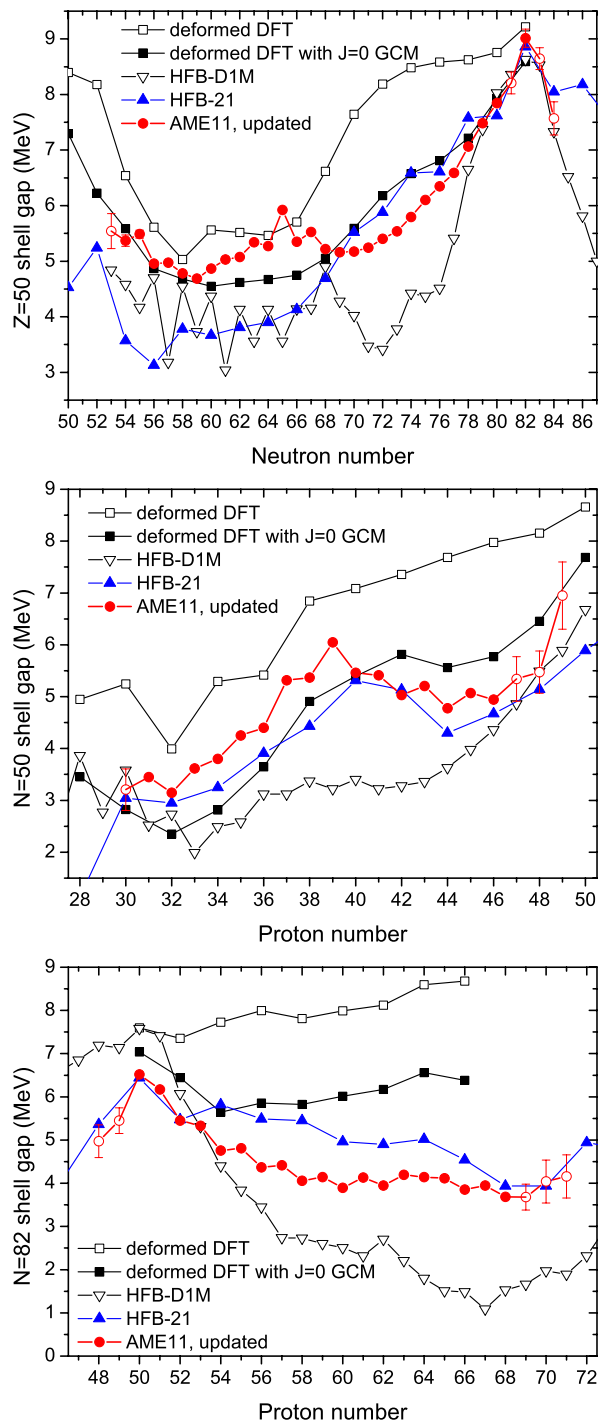
Figure 25. The $Z = 50, N = 50$ and $N = 82$ two-neutron and two-proton shell gaps as a function of neutron and proton numbers, respectively. Plotted are the most recent experimental values together with two calculations employing the SLy4 energy density functional in the deformed basis with and without dynamical quadrupole correlations [3], the most recent Skyrme HFB mean-field calculations HFB-21 [75], and Gogny HFB mass model HFB-D1M [94].
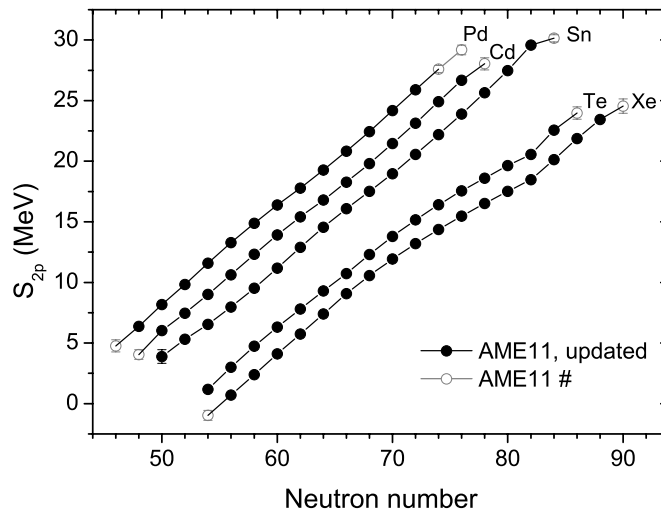
Figure 26. Two-proton separation energies as a function of neutron number for even-Z isotopes from Pd ($Z = 46$) to Xe ($Z = 54$). The gap between the Sn and Te chains shows the evolution of the $Z = 50$ shell gap from $N = 50$ to $N = 82$.

persistence of the $N = 82$ shell closure but with a reduction of about 2.5 MeV from $Z = 50$ to 58. Included in this figure are theoretical values calculated with the mean-field models of Bender *et al* [3] and Goriely *et al* [94]. The calculation of Bender *et al* employs SLy4 [81] energy density functional in the deformed basis with dynamical quadrupole correlations. A relatively good agreement with the experimental values has been obtained although the model is not able to explain the reduction sufficiently, unlike in the case of $N = 50$ [46]. The calculation without correlations gives a rather constant or slightly increasing value as a function of proton number. This confirms the importance of correlations due to core polarization.

Another similar mean-field approach of Goriely *et al* [94] employs the HFB framework with a Gogny interaction taking into account all the quadrupole correlations self-consistently and microscopically. However, this model provides too strong reduction for the energy gap with increasing Z but reproduces the gap near $Z = 50$ equally well with the other two calculations. In conclusion, it is obvious that the mean-field models such as those in [3, 94] rather successfully describe the binding energies near the shell closure. At $Z = 50$ and $N = 82$ the over-prediction of the gap is only about 0.5 MeV. Our present mass data provide no information on the behaviour of the $N = 82$ shell closure below Sn which remains a major challenge for future experiments.

Of equal importance in probing the possible shell evolution outside of the doubly magic ^{132}Sn is the systematics of two-proton separation energies. They are plotted for five isotopic chains around $Z = 50$ in figure 26. The gap is well pronounced at $N = 82$ and is about twice larger than the gap in the middle of the shell signalling the importance of mutual magicity in ^{132}Sn binding. The changing energy gap highlights the role of correlations along the isotopic chain as seen in figure 25 where a comparison is made against the model calculations with and without correlations.

4.3. Nucleon binding energy and proton–neutron pairing

4.3.1. Odd–even effects in neutron separation energies.   Single nucleon binding energy is not of interest only for mapping the neutron- and proton drip lines in defining the limits of nuclear
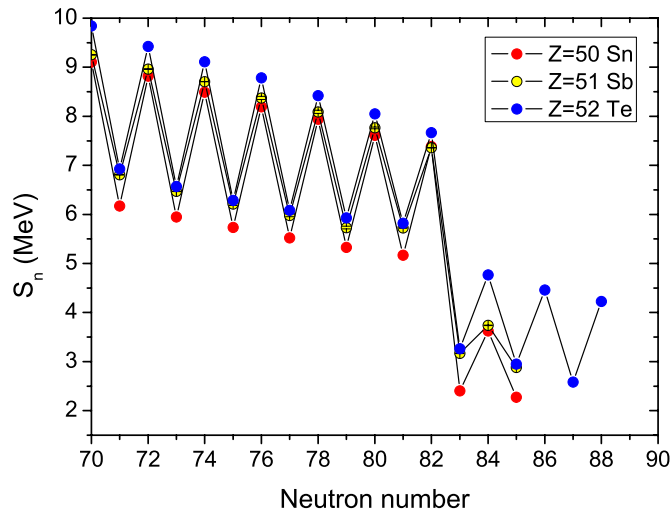
Figure 27. Neutron separation energy as a function of neutron number for Sn, Sb, and Te isotopes.

existence, but their variations with proton and neutron numbers contain also information on valence particle properties of ground states and are characterized by pairing effects due to *pp*, *nn* and *pn* interaction. The latter has a relatively weak effect on binding energy. Therefore, their study requires highest possible accuracies for the mass measurements. As an example, we show one-neutron separation energy for Sn, Sb and Te isotopes as a function of the neutron number in figure 27. In addition to the large drop in binding between $N = 82$ and $N = 83$, the curves are characterized by the prevailing odd–even effects. In particular, the proton–neutron pairing effect seen as an increased binding of odd–odd isotopes is obvious. For example, by adding a proton to the odd-neutron nucleus ^{133}Sn increases its neutron binding energy by about 0.8 MeV. To demonstrate the effect, we plotted neutron separation energies for the $N = 83$ as a function of proton number (see figure 28). This phenomenon is common over the entire nuclear mass table and has not been treated/solved by any systematic theory so far.

A possible explanation for the increased binding was offered by Friedman and Bertsch [98] within the density functional theory, at its spherical or strongly deformed limit. In the spherical limit the odd-neutron goes into spherical j_n shell with an energy of ϵ_n and proton to a j_p shell. The enhancement due *pn* pairing can now be estimated empirically from the spectrum of the odd–odd nucleus as:

$$\delta_S = \sum_{J=|j_n-j_p|}^{J=|j_n+j_p|} (2J+1)E_J(2j_n+1)(2j_p+1).$$ (4)

Here E_J are the measured energies of the levels of the multiplet in the odd–odd nucleus. One of the best examples to test this formulation is ^{134}Sb where all the members of the $\pi g_{7/2}\nu f_{7/2}$ multiplet from the 0^- ground state to the 7^- isomer at 279 keV are known [34]. Employing the above formula we get the empirical value of 0.48 MeV for δ_s. This should be compared with the value extracted from the neutron separation energies of nuclei with proton numbers Z, $Z + 1$ and $Z + 2$. Following the procedure of [98] and standard angular momentum recoupling results in the value of 0.43 MeV in excellent agreement with the empirical shell-model estimate.
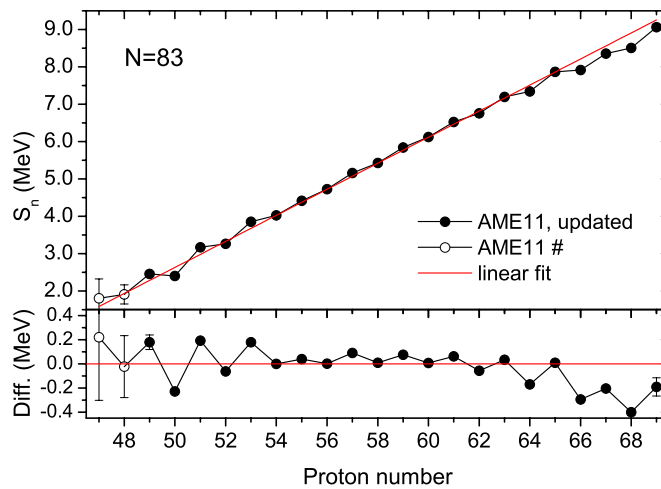
Figure 28. Neutron separation energies for the $N = 83$ isotones as a function of proton number. A linear fit has been plotted to highlight the zigzag trend. The differences between the data points and the linear fit are shown in the lower panel. The odd-Z isotones have higher neutron binding energies compared to their neighbouring even-Z nuclei.
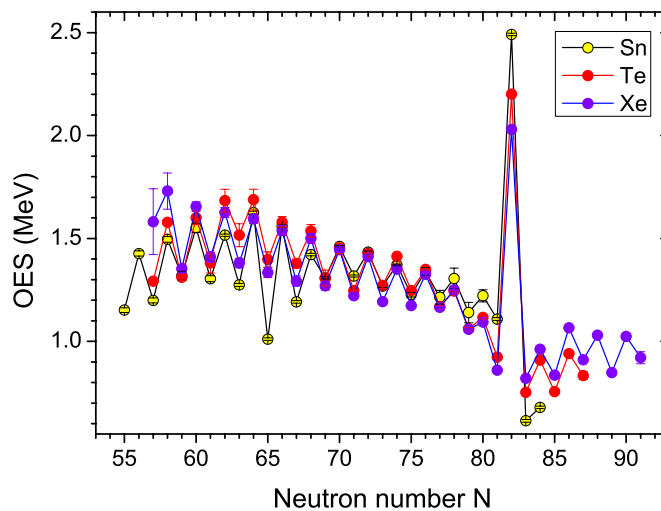

Figure 29. OES as a function of neutron number for Sn, Te, and Xe isotopes.

4.3.2. Odd–even staggering of masses and pairing gap. High-accuracy mass measurements with Penning traps are opening a new vision for studies of fine structure effects in nuclear binding energies. An excellent and important application is the study of pairing effects which represent relative contribution to a total mass energy in the level of the order of 10^{-5} to 10^{-6}. Pairing energy gaps gain particular importance in weakly bound nuclei far from the valley of stability. Their formulation represents an important task for nuclear theory. Empirically, pairing energies can be studied by measuring odd-even mass differences along the isotopic or isotonic chains. OES has been largely attributed to BCS pairing but there are also other mechanisms, such as those due to mean-field effects, that can contribute (see e.g. [4, 99–101]).
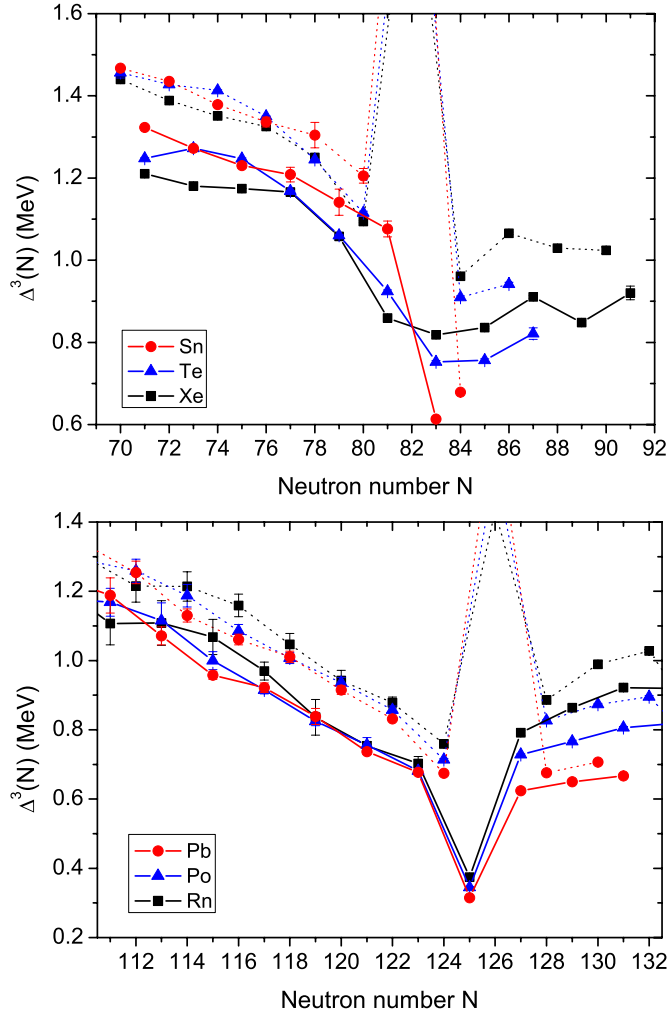
Figure 30. Neutron OES across the $N = 82$ and $N = 126$ shell closures. The odd-N and even-N isotopes are connected with solid and dashed lines, respectively.

The simplest approach for studying the pairing effect is the three-point odd–even mass staggering formula, written here for neutrons:

$$\Delta_N^{(3)} = (-1)^N \left[ME(Z, N + 1) - 2ME(Z, N) + ME(Z, N - 1) \right] / 2, \qquad (5)$$

where ME is mass excess and Z and N denote proton and neutron numbers. One advantage of this formula is that it can be applied to more experimental data than the higher order formulae. As pointed out in the above mentioned references the three-point formula presents contributions from both pairing and mean-field effects. The odd-neutron values of $\Delta_N^{(3)}$ can be considered to be a measure of pairing effects only whereas the even-N values are more sensitive to the splitting of the single-particle spectrum around the Fermi level [4, 101].

Figure 29 presents $\Delta_N^{(3)}$ for Sn, Te and Xe isotopes and shows a rather uniform overall pattern and odd–even variation. For Sn isotopes the small dip at $N = 65$ and the large one at $N = 83$ could be attributed to a neutron subshell at $N = 64$ and the neutron shell closure at $N = 82$. The mean-field calculations of [102] employing the pairing functional with mixed
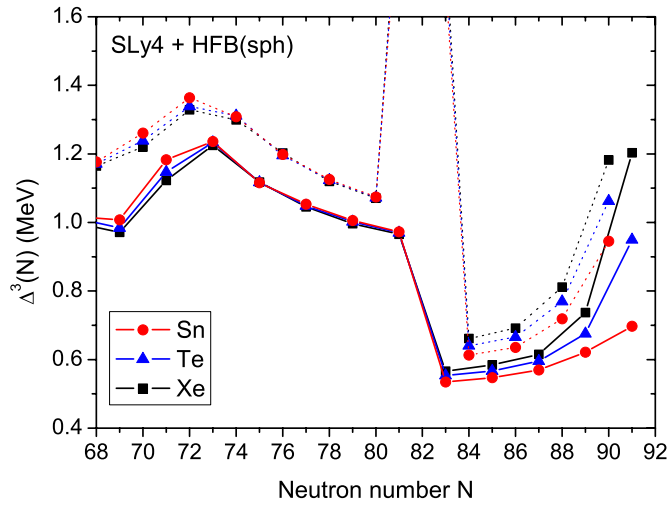
Figure 31. Odd–even mass staggering for Sn, Te, and Xe isotope chains calculated with spherical HFB. The odd and even isotopes are connected with solid and dashed lines, respectively.

surface and volume pairing were able to reproduce the overall trend of OES for Sn isotopes rather well up to ^{133}Sn. No results were presented for Te or Xe isotopes in this reference. However, their behaviour is similar to Sn except above $N = 82$. It is obvious that there is an asymmetry in the OES values when crossing the $N = 82$ shell closure.

To highlight the asymmetry across $N = 82$ the experimental neutron OES for Sn, Te, and Xe isotopes is shown in figure 30. To emphasize pairing effects, for each isotopic chain the points with odd neutron numbers are connected by solid lines. The difference between the values for $N = 81$ and 83 shows a large asymmetry for Sn but a much smaller one for Te and Xe. For comparison we show in the lower part of figure 30 the OES for Pb and Po isotopes across $N = 126$. Here the symmetric behaviour is obvious around $N = 125$. Contrary to this, the upper figure indicates a considerably stronger quenching in pairing gap for Sn than for Te and Xe suggesting importance of core polarization effects. This is in somewhat discrepant to the behaviour of the shell gap energy shown in figure 25. Therefore this behaviour remains somewhat puzzling. However, concerning the question of asymmetry itself, it is of interest to note that a similar asymmetry has been observed for the $B(E2)$ values of neutron-rich Te isotopes. It was also traced to reduced neutron pairing above the $N = 82$ shell closure [103].

In order to probe this question theoretically self-consistent calculations were recently performed by using the Sly4 [104] energy density functional and contact pairing force. The pairing channel was described within the HFB approximation and the blocking and filling approximations [101, 105] were used to treat odd nuclei. Figure 31 shows the neutron $\Delta_N^{(3)}$ staggering calculated within the spherical approximation [106]. The experimental decrease of OES when crossing the $N = 82$ gap in Sn is very well reproduced with the volume or mixed pairing forces [107], whereas the data exclude the pure surface-localized pairing force. As discussed in a previous paper [103], such pairing decrease is due to a lower level density above the $N = 82$ gap. However, in the $N = 83$ isotones, the disagreement with data for Te and Xe remains a puzzle, unresolved within the current state of the art theoretical approaches. It cannot be explained by the combined pairing and static-deformation correlation effects. Study of higher-order correlations, such as the configuration mixing of deformed states, requires an implementation of methods for odd nuclei that are presently not available, see [49].
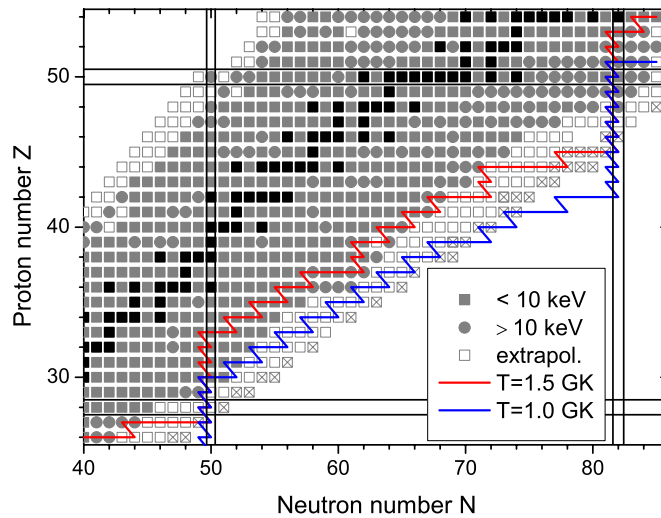
Figure 32. Chart of the nuclides showing the uncertainties related to mass-excess values [17, 48, 49] and two different r-process paths [113, 114] for conditions $T = 1.5$ GK and $N_n = 10^{24}$ cm^{-3} and $T = 1.0$ GK and $N_n = 10^{28}$ cm^{-3}. The new nuclei identified recently at RIKEN [18] are denoted by grey crosses.

4.4. Nuclear astrophysics

Masses play a key role in the modelling of the astrophysical r process since they affect neutron-capture, beta-decay and photodisintegration rates as well as fission probabilities of the involved nuclei [108–112]. Therefore, masses have to be known accurately enough in order to reliably compare the calculated r-process abundances to the observations. In the region of the studied fission fragments (see figure 32), the r process moves along the $N = 50$ neutron shell via subsequent beta decays and neutron captures up to around $Z = 30$. Then, it runs away towards more neutron-rich nuclei until it reaches the neutron shell $N = 82$ after around $Z = 40$. The r-process path depends strongly on the used astrophysical model and the environment (temperature and neutron density). If fission and the resulting cycling of the matter is taken into account, more nuclides in a broader region are involved in the process.

Penning-trap mass measurements have reached the r-process path for nuclides around ^{80}Zn$_{50}$ and ^{132}Sn$_{82}$. More than 50 nuclides, whose masses have been measured either with JYFLTRAP or ISOLTRAP, are located at the r-process path ($T = 1.5$ GK, $N_n = 10^{24}$ cm^{-3}) plotted in red in figure 32. As a result, the uncertainties of the mass-excess values in the AME11 have been reduced below 10 keV for most of these nuclides. Although many of the r-process nuclei will remain unreachable for current facilities, the large number and superior precision of Penning-trap mass measurements help in constructing more reliable mass extrapolations and models to be used for r-process studies.

Isomeric states have to be taken into account in the r-process modelling. Namely, isomers and low-lying excited states can be thermally populated if the r-process operates at high temperatures, and thus, the beta-decay rates can be significantly different from the terrestrial rates [112]. On the other hand, if the r-process operates at such low temperatures that thermal equilibrium cannot be achieved, it becomes necessary to independently describe the population of different isomers after neutron capture and the rates for neutron capture and decay of each isomer. Mass uncertainties related to nuclei having isomers can be reduced via post-trap decay

spectroscopy which helps in identifying the measured state as the ground state or an isomer or a mixture of states.

5. Conclusions

High-precision Penning-trap mass measurements of fission fragments have increased our knowledge of neutron-rich nuclei and their properties. The measurements have also been accurate: results obtained at different Penning-trap facilities agree generally well with each other. Typically, neutron-rich nuclei have been found to be less bound than evaluated in AME03. The deviation accumulates when moving towards more neutron-rich nuclei. Penning traps provide also a new way to measure masses or excitation energies of isomeric states. The precisely measured masses of fission fragments and their derivatives have been essential for studying e.g. evolution of shell gaps, deformation, OES and pairing effects. New mass data offer also a good database to test different theoretical mass models. Accurate mass values and theoretical estimates are needed for more reliable modelling of the astrophysical *r*-process. In future, Penning traps aim towards more exotic neutron-rich nuclei. They are also essential facilities to purify radioactive beams for spectroscopic studies of neutron-rich nuclei.

Acknowledgments

References

[1] Lunney D, Pearson J M and Thibault C 2003 Recent trends in the determination of nuclear masses *Rev. Mod. Phys.* **75** 1021–82
[2] Blaum K 2006 High-accuracy mass spectrometry with stored ions *Phys. Rep.* **425** 1–78
[3] Bender M, Bertsch G F and Heenen P-H 2006 Global study of quadrupole correlation effects *Phys. Rev.* C **73** 034322
[4] Satuła W, Dobaczewski J and Nazarewicz W 1998 Odd–even staggering of nuclear masses: pairing or shape effect? *Phys. Rev. Lett.* **81** 3599–602
[5] Zhang J-Y, Casten R F and Brenner D S 1989 Empirical proton–neutron interaction energies. Linearity and saturation phenomena *Phys. Lett.* B **227** 1–5
[6] Van Isacker P, Warner D D and Brenner D S 1995 Test of Wigner's spin-isospin symmetry from double binding energy differences *Phys. Rev. Lett.* **74** 4607–10
[7] Cakirli R B, Brenner D S, Casten R F and Millman E A 2005 Proton–neutron interactions and the new atomic masses *Phys. Rev. Lett.* **94** 092501
[8] Neidherr D *et al* 2009 High-precision Penning-trap mass measurements of heavy xenon isotopes for nuclear structure studies *Phys. Rev.* C **80** 044323
[9] Peräjärvi K *et al* 2010 Ultra-high resolution mass separator—application to detection of nuclear weapons tests *Appl. Radiat. Isot.* **68** 450–3
[10] Savard G, Becker S, Bollen G, Kluge H J, Moore R B, Otto T, Schweikhard L, Stolzenberg H and Wiess U 1991 A new cooling technique for heavy ions in a Penning trap *Phys. Lett.* A **158** 247–52
[11] Kugler E 2000 The ISOLDE facility *Hyperfine Interact.* **129** 23–42
[12] Äystö J 2001 Development and applications of the IGISOL technique *Nucl. Phys.* A **693** 477–94
[13] Mukherjee M *et al* 2008 ISOLTRAP: An on-line Penning trap for mass spectrometry on short-lived nuclides *Eur. Phys. J.* A **35** 1–29
[14] Kolhinen V S *et al* 2004 JYFLTRAP: a cylindrical Penning trap for isobaric beam purification at IGISOL *Nucl. Instrum. Methods Phys. Res.* A **528** 776–87
[15] Jokinen A *et al* 2006 Experimental studies at JYFLTRAP *Hyperfine Interact.* **173** 143–51

[16] Eronen T *et al* 2012 JYFLTRAP: a Penning trap for precision mass spectroscopy and isobaric purification *Eur. Phys. J.* A **48** 46

[17] Audi G and Wang M 2011 Preview of AME2013 and NUBASE2013 private communication

[18] Ohnishi T *et al* 2010 Identification of 45 new neutron-rich isotopes produced by in-flight fission of a ^{238}U beam at 345 MeV/nucleon *J. Phys. Soc. Japan* **79** 073201

[19] Karvonen P, Moore I D, Sonoda T, Kessler T, Penttilä H, Peräjärvi K, Ronkanen P and Äystö J 2008 A sextupole ion beam guide to improve the efficiency and beam quality at IGISOL *Nucl. Instrum. Methods Phys. Res.* B **266** 4794–807

[20] Nieminen A, Huikari J, Jokinen A, Äystö J, Campbell P and Cochrane E C A 2001 Beam cooler for low-energy radioactive ions *Nucl. Instrum. Methods Phys. Res.* A **469** 244–53

[21] Wang J C *et al* 2004 The Canadian Penning trap mass spectrometer *Nucl. Phys.* A **746** 651–4

[22] Ringle R, Bollen G, Prinke A, Savory J, Schury P, Schwarz S and Sun T 2009 The LEBIT 9.4 T Penning trap mass spectrometer *Nucl. Instrum. Methods Phys. Res.* A **604** 536–47

[23] Simon V V *et al* 2012 Penning-trap mass spectrometry of highly charged, neutron-rich Rb and Sr isotopes in the vicinity of A≈100 *Phys. Rev.* C **85** 064308

[24] Dilling J 2010 Report on recent activities at the TITAN mass spectrometer at ISAC/TRIUMF *Hyperfine Interact.* **196** 219–23

[25] Brown L S and Gabrielse G 1986 Geonium theory: physics of a single electron or ion in a Penning trap. *Rev. Mod. Phys.* **58** 233–311

[26] Karvonen P *et al* 2008 Upgrade and yields of the IGISOL facility *Nucl. Instrum. Methods Phys. Res.* B **266** 4454–9

[27] Penttilä H *et al* 2010 Determining isotopic distributions of fission products with a Penning trap *Eur. Phys. J.* A **44** 147–68

[28] Eronen T, Elomaa V-V, Hager U, Hakala J, Jokinen A, Kankainen A, Rahaman S, Rissanen J, Weber C and Äystö J 2008 Preparing isomerically pure beams of short-lived nuclei at JYFLTRAP *Nucl. Instrum. Methods Phys. Res.* B **266** 4527–31

[29] Ramsey N F 1990 Experiments with separated oscillatory fields and hydrogen masers *Rev. Mod. Phys.* **62** 541–52

[30] Bollen G, Kluge H-J, Otto T, Savard G and Stolzenberg H 1992 Ramsey technique applied in a Penning trap mass spectrometer *Nucl. Instrum. Methods Phys. Res.* B **70** 490–3

[31] Kretzschmar M 2007 The Ramsey method in high-precision mass spectrometry with Penning traps: theoretical foundations *Int. J. Mass Spectrom.* **264** 122–45

[32] Gräff G, Kalinowsky H and Traut J 1980 A direct determination of the proton electron mass ratio *Z. Phys.* A **297** 35–9

[33] König M, Bollen G, Kluge H J, Otto T and Szerypo J 1995 Quadrupole excitation of stored ion motion at the true cyclotron frequency *Int. J. Mass Spectrom. Ion Process.* **142** 95–116

[34] Shergur J *et al* 2005 Level structure of odd–odd ^{134}Sb populated in the β^- decays of ^{134,135}Sn *Phys. Rev.* C **71** 064321

[35] George S, Blaum K, Herfurth F, Herlert A, Kretzschmar M, Nagy S, Schwarz S, Schweikhard L and Yazidjian C 2007 The Ramsey method in high-precision mass spectrometry with Penning traps: experimental results *Int. J. Mass Spectrom.* **264** 110–21

[36] Eronen T *et al* 2009 Q_{EC} values of the superallowed β emitters ^{34}Cl and ^{38}K^m *Phys. Rev. Lett.* **103** 252501

[37] Kellerbauer A, Blaum K, Bollen G, Herfurth F, Kluge H-J, Kuckein M, Sauvan E, Scheidenberger C and Schweikhard L 2003 From direct to absolute mass measurements: a study of the accuracy of ISOLTRAP *Eur. Phys. J.* D **22** 53–64

[38] Birge R T 1932 The calculation of errors by the method of least squares *Phys. Rev.* **40** 207–227

[39] Elomaa V-V, Eronen T, Hakala J, Jokinen A, Kankainen A, Moore I D, Rahaman S, Rissanen J, Weber C and Äystö J 2009 Systematic studies of the accuracy of the penning trap mass spectrometer JYFLTRAP *Nucl. Instrum. Methods Phys. Res.* A **612** 97–102

[40] Hager U *et al* 2006 First precision mass measurements of refractory fission fragments *Phys. Rev. Lett.* **96** 042504

[41] Hager U *et al* 2007 Precision mass measurements of neutron-rich yttrium and niobium isotopes *Nucl. Phys.* A **793** 20–39

[42] Hager U *et al* 2007 Precision mass measurements of neutron-rich Tc, Ru, Rh, and Pd isotopes *Phys. Rev.* C **75** 064302

[43] Rahaman S *et al* 2007 Precise atomic masses of neutron-rich Br and Rb nuclei close to the *r*-process path *Eur. Phys. J.* A **32** 87–96

[44] Rahaman S *et al* 2007 Masses of neutron-rich Ni and Cu isotopes and the shell closure at $Z = 28$, $N = 40$ *Eur. Phys. J.* A **34** 5–9

[45] Rinta-Antila S *et al* 2007 Decay study of neutron-rich zirconium isotopes employing a Penning trap as a spectroscopy tool *Eur. Phys. J.* A **31** 1–7

[46] Hakala J *et al* 2008 Evolution of the $N = 50$ shell gap energy towards ^{78}Ni *Phys. Rev. Lett.* **101** 052502

[47] Wieslander J S E *et al* 2009 Smallest known Q value of any nuclear decay: the rare β^- decay of ^{115}In $(9/2^+) \rightarrow ^{115}Sn(3/2^+)$ *Phys. Rev. Lett.* **103** 122501

[48] Hakala J *et al* 2011 Precision mass measurements of neutron-rich Y, Nb, Mo, Tc, Ru, Rh, and Pd isotopes *Eur. Phys. J.* A **47** 129

[49] Hakala J *et al* 2012 Precision mass measurements beyond ^{132}Sn: anomalous behaviour of odd–even staggering of binding energies *Phys. Rev. Lett.* arXiv:1203.0958v3 [nucl-ex]

[50] Kankainen A *et al* 2012 Isomeric states close to doubly magic ^{132}Sn studied with JYFLTRAP *Phys. Rev.* C arXiv:1206.6236v1 [nucl-ex]

[51] Stolzenberg H, Becker S, Bollen G, Kern F, Kluge H-J, Otto T, Savard G, Schweikhard L, Audi G and Moore R B 1990 Accurate mass determination of short-lived isotopes by a tandem Penning-trap mass spectrometer *Phys. Rev. Lett.* **65** 3104–7

[52] Ames F *et al* 1999 High-accuracy mass determination of unstable cesium and barium isotopes *Nucl. Phys.* A **651** 3–30

[53] Raimbault-Hartmann H *et al* 2002 High-accuracy mass determination of neutron-rich rubidium and strontium isotopes *Nucl. Phys.* A **706** 3–14

[54] Van Roosbroeck J *et al* 2004 Unambiguous identification of three β-decaying isomers in ^{70}Cu *Phys. Rev. Lett.* **92** 112501

[55] Guénaut C *et al* 2005 Mass measurements of $^{56-57}$Cr and the question of shell reincarnation at $N = 32$ *J. Phys. G: Nucl. Part. Phys.* **31** S1765

[56] Sikler G *et al* 2005 Mass measurements on neutron-deficient Sr and neutron-rich Sn isotopes with the ISOLTRAP mass spectrometer *Nucl. Phys.* A **763** 45–58

[57] Delahaye P *et al* 2006 High-accuracy mass measurements of neutron-rich Kr isotopes *Phys. Rev.* C **74** 034331

[58] Guénaut C *et al* 2007 High-precision mass measurements of nickel, copper, and gallium isotopes and the purported shell closure at $N = 40$ *Phys. Rev.* C **75** 044303

[59] Weber C, Audi G, Beck D, Blaum K, Bollen G, Herfurth F, Kellerbauer A, Kluge H-J, Lunney D and Schwarz S 2008 Atomic mass measurements of short-lived nuclides around the doubly-magic ^{208}Pb *Nucl. Phys.* A **803** 1–29

[60] Baruah S *et al* 2008 Mass measurements beyond the major r-process waiting point ^{80}Zn *Phys. Rev. Lett.* **101** 262501

[61] Dworschak M *et al* 2008 Restoration of the $N = 82$ shell gap from direct mass measurements of ^{132,134}Sn *Phys. Rev. Lett.* **100** 072501

[62] Naimi S *et al* 2010 Critical-point boundary for the nuclear quantum phase transition near $A = 100$ from mass measurements of ^{96,97}Kr *Phys. Rev. Lett.* **105** 032502

[63] Breitenfeldt M *et al* 2010 Approaching the $N = 82$ shell closure with mass measurements of Ag and Cd isotopes *Phys. Rev.* C **81** 034313

[64] Savard G *et al* 2006 Studies of neutron-rich isotopes with the CPT mass spectrometer and the CARIBU project *Int. J. Mass Spectrom.* **251** 252–9

[65] Van Schelt J *et al* 2012 Mass measurements near the r-process path using the Canadian Penning Trap mass spectrometer *Phys. Rev.* C **85** 045805

[66] Ferrer R *et al* 2010 Penning trap mass spectrometry of neutron-rich Fe and Co isotopes around $N = 40$ with the LEBIT mass spectrometer *Phys. Rev.* C **81** 044318

[67] JYFLTRAP mass database: http://research.jyu.fi/igisol/JYFLTRAP_masses/

[68] ISOLTRAP database: http://isoltrap.web.cern.ch/isoltrap/database/isodb.asp

[69] Blaum K *et al* 2004 Population inversion of nuclear states by a Penning trap mass spectrometer *Europhys. Lett.* **67** 586

[70] Hardy J C, Carraz L C, Jonson B and Hansen P G 1977 The essential decay of pandemonium: a demonstration of errors in complex beta-decay schemes *Phys. Lett.* B **71** 307–10

[71] Audi G, Wapstra A H and Thibault C 2003 The 2003 atomic mass evaluation: II. Tables, graphs and references *Nucl. Phys.* A **729** 337–676

[72] Audi G, Bersillon O, Blachot J and Wapstra A H 2003 The evaluation of nuclear and decay properties *Nucl. Phys.* A **729** 3–128

[73] Möller P, Nix J R, Myers W D and Swiatecki W J 1995 Nuclear ground-state masses and deformations *At. Data Nucl. Data Tables* **59** 185–381

[74] Duflo J and Zuker A P 1995 Microscopic mass formulas *Phys. Rev.* C **52** R23–7

[75] Goriely S, Chamel N and Pearson J M 2010 Further explorations of Skyrme–Hartree–Fock–Bogoliubov mass formulas: XII. Stiffness and stability of neutron-star matter *Phys. Rev.* C **82** 035804

[76] Stoitsov M V, Dobaczewski J, Nazarewicz W, Pittel S and Dean D J 2003 Systematic study of deformed nuclei at the drip lines and beyond *Phys. Rev.* C **68** 054312

[77] Stoitsov M V, Dobaczewski J, Nazarewicz W and Borycki P 2006 Large-scale self-consistent nuclear mass calculations *Int. J. Mass Spectrom.* **251** 243–51

[78] Dobaczewski J, Stoitsov M V and Nazarewicz W 2004 Skyrme-HFB deformed nuclear mass table *AIP Conf. Proc.* **726** 51 (arXiv:nucl-th/0404077)

[79] Heyde Kris and Wood J L 2011 Shape coexistence in atomic nuclei *Rev. Mod. Phys.* **83** 1467–521

[80] Lhersonneau G *et al* 1994 Evolution of deformation in the neutron-rich Zr region from excited intruder state to the ground state *Phys. Rev.* C **49** 1379–90

[81] Charlwood F C *et al* 2009 Nuclear charge radii of molybdenum fission fragments *Phys. Lett.* B **674** 23–7

[82] Takahara S, Onishi N, Shimizu Y R and Tajima N 2011 The role of spin–orbit potential in nuclear prolate-shape dominance *Phys. Lett.* B **702** 429–32

[83] Weizsäcker C F v 1935 Zur Theorie der Kernmassen *Z. Phys.* A **96** 431–58

[84] Bethe H A and Bacher R F 1936 Nuclear physics A. Stationary states of nuclei *Rev. Mod. Phys.* **8** 82–229

[85] Fossion R, De Coster C, García-Ramos J E, Werner T and Heyde K 2002 Nuclear binding energies: global collective structure and local shell-model correlations *Nucl. Phys.* A **697** 703–47

[86] Delaroche J P, Girod M, Libert J, Goutte H, Hilaire S, Péru S, Pillet N and Bertsch G F 2010 Structure of even–even nuclei using a mapped collective Hamiltonian and the D1S Gogny interaction *Phys. Rev.* C **81** 014303

[87] Nikšić T, Li Z P, Vretenar D, Próchniak L, Meng J and Ring P 2009 Beyond the relativistic mean-field approximation. III. Collective Hamiltonian in five dimensions *Phys. Rev.* C **79** 034303

[88] Vingerhoets P *et al* 2010 Nuclear spins, magnetic moments, and quadrupole moments of Cu isotopes from $N = 28$ to $N = 46$: probes for core polarization effects *Phys. Rev.* C **82** 064311

[89] Otsuka T, Suzuki T, Fujimoto R, Grawe H and Akaishi Y 2005 Evolution of nuclear shells due to the tensor force *Phys. Rev. Lett.* **95** 232502

[90] Cheal B *et al* 2010 Nuclear spins and moments of Ga isotopes reveal sudden structural changes between $N = 40$ and $N = 50$ *Phys. Rev. Lett.* **104** 252502

[91] Otsuka T, Matsuo T and Abe D 2006 Mean field with tensor force and shell structure of exotic nuclei *Phys. Rev. Lett.* **97** 162501

[92] Otsuka T 2008 private communication

[93] Zeldes N, Dumitrescu T S and Köhler H S 1983 Mutual support of magicities and residual effective interactions near ^{208}Pb *Nucl. Phys.* A **399** 11–50

[94] Goriely S, Chamel N and Pearson J M 2009 Skyrme–Hartree–Fock–Bogoliubov nuclear mass formulas: crossing the 0.6 MeV accuracy threshold with microscopically deduced pairing *Phys. Rev. Lett.* **102** 152503

[95] Sieja K and Nowacki F 2010 Shell quenching in ^{78}Ni: a hint from the structure of neutron-rich copper isotopes *Phys. Rev.* C **81** 061303

[96] Hoff P *et al* 1996 Single-neutron states in ^{133}Sn *Phys. Rev. Lett.* **77** 1020–3

[97] Jones K L *et al* 2010 The magic nature of ^{132}Sn explored through the single-particle states of ^{133}Sn *Nature* **465** 454–7

[98] Friedman W A and Bertsch G F 2007 Neutron–proton pairing reexamined *Phys. Rev.* C **76** 057301

[99] Dobaczewski J, Magierski P, Nazarewicz W, Satuła W and Szymański Z 2001 Odd–even staggering of binding energies as a consequence of pairing and mean-field effects *Phys. Rev.* C **63** 024308

[100] Duguet T, Bonche P, Heenen P-H and Meyer J 2001 Pairing correlations: II. Microscopic analysis of odd–even mass staggering in nuclei *Phys. Rev.* C **65** 014311

[101] Bertsch G, Dobaczewski J, Nazarewicz W and Pei J 2009 Hartree–Fock–Bogoliubov theory of polarized Fermi systems *Phys. Rev.* A **79** 043602

[102] Bertulani C A, Lü H F and Sagawa H 2009 Odd–even mass difference and isospin dependent pairing interaction *Phys. Rev.* C **80** 027303

[103] Terasaki J, Engel J, Nazarewicz W and Stoitsov M 2002 Anomalous behavior of 2^+ excitations around ^{132}Sn *Phys. Rev.* C **66** 054313

[104] Chabanat E, Bonche P, Haensel P, Meyer J and Schaeffer R 1998 A Skyrme parametrization from subnuclear to neutron star densities part II. nuclei far from stabilities *Nucl. Phys.* A **635** 231–56

[105] Schunck N, Dobaczewski J, McDonnell J, Moré J, Nazarewicz W, Sarich J and Stoitsov M V 2010 One-quasiparticle states in the nuclear energy density functional theory *Phys. Rev.* C **81** 024316

[106] Dobaczewski J, Flocard H and Treiner J 1984 Hartree–Fock–Bogolyubov description of nuclei near the neutron-drip line *Nucl. Phys.* A **422** 103–39

[107] Dobaczewski J, Nazarewicz W and Stoitsov M V 2002 Nuclear ground-state properties from mean-field calculations *Eur. Phys. J.* A **15** 21–6

[108] Arnould M and Takahashi K 1999 Nuclear astrophysics *Rep. Prog. Phys.* **62** 395

[109] Pfeiffer B, Kratz K-L, Thielemann F-K and Walters W B 2001 Nuclear structure studies for the astrophysical *r*-process *Nucl. Phys.* A **693** 282–324

[110] Wanajo S, Goriely S, Samyn M and Itoh N 2004 The *r*-process in supernovae: impact of new microscopic mass formulae *Astrophys. J.* **606** 1057

[111] Schatz H 2006 The importance of nuclear masses in the astrophysical *rp*-process *Int. J. Mass Spectrom.* **251** 293–9

[112] Arnould M, Goriely S and Takahashi K 2007 The *r*-process of stellar nucleosynthesis: astrophysics and nuclear physics achievements and mysteries *Phys. Rep.* **450** 97–213

[113] Seeger P A, Fowler W A and Clayton D D 1965 Nucleosynthesis of heavy elements by neutron capture *Astrophys. J. Suppl. Ser.* **11** 121

[114] Bouquelle V, Cerf N, Arnould M, Tachibana T and Goriely S 1996 Single and multi-event canonical *r*-process: astrophysics and nuclear physics considerations *Astron. Astrophys.* **305** 1005 (available at http://articles.adsabs.harvard.edu/cgi-bin/nph-iarticle_query?1996A%26A...305.1005B&data_type=PDF_HIGH&whole_paper=YES&type=PRINTER&filetype=.pdf)